Transportation Consortium of South-Central States

Solving Emerging Transportation Resiliency, Sustainability, and Economic Challenges through the Use of Innovative Materials and Construction Methods: From Research to Implementation

Rapid Repair of Cracks on the Embankment Slopes Using Bio-Cement

Project No. 20GTLSU11

Lead University: Louisiana State University

TECHNICAL DOCUMENTATION PAGE

1. Project No. 20GTLSU11	2. Government Accession No.	3. Recipient's Catalog No.		
4. Title and Subtitle Rapid Repair of Cracks on the Embankment Slopes Using Bio-Cement		**5. Report Date** Oct. 2021		
		6. Performing Organization Code		
7. Author(s) PI: Hai Lin https://orcid.org/0000-0002-1641-4588 GRA: Guantao Cheng https://orcid.org/0000-0002-2102-4672		**8. Performing Organization Report No.**		
9. Performing Organization Name and Address Transportation Consortium of South-Central States (Tran-SET)		**10. Work Unit No. (TRAIS)**		
University Transportation Center for Region 6 3319 Patrick F. Taylor Hall, Louisiana State University, Baton Rouge, LA 70803		**11. Contract or Grant No.** 69A3551747106		
12. Sponsoring Agency Name and Address United States of America Department of Transportation Research and Innovative Technology Administration		**13. Type of Report and Period Covered** Final Research Report Aug. 2020 – Aug. 2021		
		14. Sponsoring Agency Code		
15. Supplementary Notes Report uploaded and accessible at Tran-SET's website (http://transet.lsu.edu/).				

16. Abstract

This research explored the feasibility of using Microbially Induced Carbonate Precipitation (MICP) to improve fine-grained soil mechanical properties, seal the soil cracks, and assess the improvement of MICP on slope stability. The conducted research tasks include (1) direct shear tests to investigate the mechanical behavior and biogeochemical reactions of low-plasticity silt treated by MICP, (2) cyclic wetting-drying tests to assess the feasibility of using MICP to seal and waterproof the soil cracks, and (3) SLOPE/W modeling of a slope treated by MICP. Direct shear tests were used to evaluate the shear responses of the low-plasticity silt under different overburden pressures (12, 25, and 35 kPa) and different bio-cement treatments. A series of cyclic wetting-drying tests were used to assess the effectiveness of MICP treatment on healing soil cracks. Crack lengths, area, width, and area percentage were measured and compared before and after the MICP treatment. SLOPE/W analysis was performed to assess the factor of safety of a slope under MICP treatment. The direct shear tests results show that the peak shear strengths increased by an average of 30% from the untreated to the MICP-treated soil samples. The wetting-drying cycle tests results show that MICP treatment can heal desiccation cracks, reducing crack length, crack width, and crack area. The results of the SLOPE/W modeling show that the MICP treatment had a positive effect on the improvement of slope stability, but more field tests are needed for optimizing the treatment solutions and procedures and assessing the long-term effect and ecological impacts.

17. Key Words Microbially induced carbonate precipitation, soil cracks, embankment slope, bio-cement		**18. Distribution Statement** No restrictions. This document is available through the National Technical Information Service, Springfield, VA 22161.		
19. Security Classif. (of this report) Unclassified	**20. Security Classif. (of this page)** Unclassified		**21. No. of Pages** 38	**22. Price**

Form DOT F 1700.7 (8-72)   **Reproduction of completed page authorized.**

SI* (MODERN METRIC) CONVERSION FACTORS

APPROXIMATE CONVERSIONS TO SI UNITS

Symbol	When You Know	Multiply By	To Find	Symbol
		LENGTH		
in	inches	25.4	millimeters	mm
ft	feet	0.305	meters	m
yd	yards	0.914	meters	m
mi	miles	1.61	kilometers	km
		AREA		
in^2	square inches	645.2	square millimeters	mm^2
ft^2	square feet	0.093	square meters	m^2
yd^2	square yard	0.836	square meters	m^2
ac	acres	0.405	hectares	ha
mi^2	square miles	2.59	square kilometers	km^2
		VOLUME		
fl oz	fluid ounces	29.57	milliliters	mL
gal	gallons	3.785	liters	L
ft^3	cubic feet	0.028	cubic meters	m^3
yd^3	cubic yards	0.765	cubic meters	m^3
		NOTE: volumes greater than 1000 L shall be shown in m^3		
		MASS		
oz	ounces	28.35	grams	g
lb	pounds	0.454	kilograms	kg
T	short tons (2000 lb)	0.907	megagrams (or "metric ton")	Mg (or "t")
		TEMPERATURE (exact degrees)		
^oF	Fahrenheit	5 (F-32)/9 or (F-32)/1.8	Celsius	^oC
		ILLUMINATION		
fc	foot-candles	10.76	lux	lx
fl	foot-Lamberts	3.426	candela/m^2	cd/m^2
		FORCE and PRESSURE or STRESS		
lbf	poundforce	4.45	newtons	N
lbf/in^2	poundforce per square inch	6.89	kilopascals	kPa

APPROXIMATE CONVERSIONS FROM SI UNITS

Symbol	When You Know	Multiply By	To Find	Symbol
		LENGTH		
mm	millimeters	0.039	inches	in
m	meters	3.28	feet	ft
m	meters	1.09	yards	yd
km	kilometers	0.621	miles	mi
		AREA		
mm^2	square millimeters	0.0016	square inches	in^2
m^2	square meters	10.764	square feet	ft^2
m^2	square meters	1.195	square yards	yd^2
ha	hectares	2.47	acres	ac
km^2	square kilometers	0.386	square miles	mi^2
		VOLUME		
mL	milliliters	0.034	fluid ounces	fl oz
L	liters	0.264	gallons	gal
m^3	cubic meters	35.314	cubic feet	ft^3
m^3	cubic meters	1.307	cubic yards	yd^3
		MASS		
g	grams	0.035	ounces	oz
kg	kilograms	2.202	pounds	lb
Mg (or "t")	megagrams (or "metric ton")	1.103	short tons (2000 lb)	T
		TEMPERATURE (exact degrees)		
^oC	Celsius	1.8C+32	Fahrenheit	^oF
		ILLUMINATION		
lx	lux	0.0929	foot-candles	fc
cd/m^2	candela/m^2	0.2919	foot-Lamberts	fl
		FORCE and PRESSURE or STRESS		
N	newtons	0.225	poundforce	lbf
kPa	kilopascals	0.145	poundforce per square inch	lbf/in^2

TABLE OF CONTENTS

LIST OF FIGURES

LIST OF TABLES

ACRONYMS, ABBREVIATIONS, AND SYMBOLS

ASTM	American Society for Testing Materials
$CaCO_3$	Calcium Carbonate
MICP	Microbially Induced Carbonate Precipitation
OD_{600}	Optical Density of a Sample Measured at a Wavelength of 600 nm
SEM	Scanning Electron Microscope
EDS	Energy-Dispersive X-ray Spectroscopy
ATCC	American Type Culture Collection
LADOTD	Louisiana Department of Transportation and Development
USCS	Unified Soil Classification System
RSCS	Revised Soil Classification System
XRD	X-Ray Diffractometer

EXECUTIVE SUMMARY

The research explored the use of microbially induced carbonate precipitation (MICP) to improve the mechanical properties of fine-grained soil and rapidly repair soil cracks on embankment slopes. Slope failures are often induced by surface cracks on the embankment slopes. To date, most rapid repair methods for slope failures (e.g., geosynthetics, soil nails, plastic pins, and lime treatment, etc.) involve large earthwork, special installation equipment, and unique construction processes, which may require extended construction time, disturb traffic, or increase the total construction cost. This research explored the feasibility of using bio-cement (MICP) to improve soil mechanical properties, seal the soil cracks, and assess the improvement of MICP on slope stability. Most previous studies on MICP treatment have focused on sandy soils. However, limited research on MICP-treated fine-grained soils were reported, which was investigated in this study. The conducted research tasks include (1) direct shear tests to investigate the mechanical behavior and biogeochemical reactions of low-plasticity silt treated by MICP, (2) cyclic wetting-drying tests to assess the feasibility of using MICP to seal and waterproof the soil cracks, and (3) SLOPE/W modeling of a slope treated by MICP. Direct shear tests were used to evaluate the shear responses of the low-plasticity silt under different overburden pressures (12, 25, and 35 kPa) and different bio-cement treatments. A series of cyclic wetting-drying tests were used to assess the effectiveness of MICP treatment on healing soil cracks. Crack lengths, area, width, and area percentage were measured and compared before and after the MICP treatment. SLOPE/W analysis was performed to assess the factor of safety of a slope under MICP treatment. The direct shear tests results show that the peak shear strengths increased by an average of 30% from the untreated to the MICP-treated soil samples. The wetting-drying cycle tests results show that MICP treatment can heal desiccation cracks, reducing crack length, crack width, and crack area. The results of the SLOPE/W modeling show that the MICP treatment had a positive effect on the improvement of slope stability, but more field tests are needed for optimizing the treatment solutions and procedures and assessing the long-term effect and ecological impacts.

1. INTRODUCTION

Highway embankment slope failures result in road closures, damage public and private properties, and pose serious safety hazards. Many slope failures happened due to desiccation cracks induced by wetting and drying cycles (*1; 2*). Wang et al. (*3*) explored the influence of cracks on the stability of embankment slopes subjected to rainfall infiltration. Results showed that the pore water pressure distributions in the slope and the factor of safety of the slopes were affected by the presence of soil cracks. When cracks were shallow, the pore water pressure profile and factor of safety of the slopes experienced small changes. When deep cracks existed, however, pore water pressures increased significantly, and the factor of safety of the slopes decreased rapidly. To remediate embankment cracks and restore embankment slopes, several slope repair methods have been used, including geosynthetics, soil nails, retaining structures, plastic pins, surface water management, and lime treatment. Most of these methods involve large earthwork, special installation equipment, and special construction processes, which may extend the construction timeline, cause road closure, and increase project costs.

The research described in this thesis investigated an innovative slope repair method using bio-cement. Bio-cement utilizes a low-viscosity and eco-friendly bio-grout that can be easily percolated into the cracks on the slopes without the need for a pressurized pump. Bio-cement can seal, waterproof, and cement slope cracks in a relatively short time (e.g., 12 hours) due to its fast reaction rate. Thus, no special installation equipment and no special construction process are required, potentially saving construction time and cost. It is envisioned that in-situ slope repair using bio-cement could be simply achieved by percolating bio-grout into the cracks at the slope surface using several buckets of bio-grout solutions.

The bio-cementation process involves the use of microbially induced carbonate precipitation (MICP). The overall MICP reaction can be written as shown in Equation 1 (*4-6*).

$$CO(NH_2)_2 + 2H_2O + CaCl_2 \rightarrow CaCO_3 \text{ (precipitation)} + 2NH_4Cl \text{ [1]}$$

MICP treatment promotes calcium carbonate ($CaCO_3$) precipitation in the soil matrix, inducing the cementation bond formation between soil particles (*7*). In comparison to untreated soil samples, MICP-stabilized sands display greater strength (*4; 8; 9*), higher stiffness (*10; 11*), lower porosity (*4*), and lower hydraulic conductivity (*7; 9*). Most studies on MICP have focused on sandy soils (*4; 5; 12; 13*). However, the effects of the MICP treatment on fine-grained soils remain largely unexplored due to the small pore-throat size among fine-grained soil particles (*8*). Here, an experimental study was conducted to investigate the effect of MICP treatment on the fine-grained soils using direct shear tests. Direct shear tests were used to investigate the shear responses of the low-plasticity silt under different overburden pressures (12, 25, and 35 kPa) and different types of MICP treatment media. Moreover, a series of cyclic wetting-drying tests were performed to evaluate the healing capability of the MICP treatment for desiccation cracks of the low-plasticity silt. Lastly, the SLOPE/W modeling was used to assess the feasibility of using MICP treatment to enhance the factor of safety of an embankment slope model.

Although many researchers have investigated MICP treatment in sand, limited studies focused on the bio-cement improvement for fine-grained soils. Also, bio-cement treatment for healing soil cracks and for enhancing slope stability are novel methods that remain unexplored. These unexplored areas were partially investigated in this thesis.

2. OBJECTIVES

Direct shear tests to investigate the mechanical behavior and biogeochemical reactions of the low-plasticity silt treated by bio-cement (MICP). Low-plasticity silt samples were treated by different types of MICP solutions and sheared under consolidated drained direct shear test condition, which was compared to the untreated silt samples. All direct shear test samples were 63.5 mm in diameter and 31.8 mm in depth. The soil was air-dried at 100°C for 24 hours, followed by mixing with the calculated amount of deionized water to achieve the optimum water content of 9.7%. The soils were then sealed and homogenized for 18 hours. Three types of samples using different treatment solutions were investigated, including untreated, UB-treated (urea medium and bacteria), and UBC-treated (urea medium, bacteria, and cementation medium) tests. Various engineering properties, including shear stress versus horizontal displacement, vertical displacement versus horizontal displacement, equivalent calcium carbonate contents, and micro-scale structure characteristics using scanning electron microscope (SEM) and the energy-dispersive X-ray spectroscopy (EDS), were measured. Raman spectroscopy was also used to investigate the chemical changes in the silt samples after MICP treatment.

Cyclic wetting-drying tests to assess the feasibility of using bio-cement to seal and waterproof soil cracks. To investigate the healing capability of the MICP treatment on the desiccation cracks, a series of cyclic wetting-drying tests were conducted. The silt was air-dried and passed through sieve No. 16 and then mixed with deionized water to achieve the liquid limit (water content = 42%). The prepared silt was poured into 150 mm diameter Petri dishes, compacted, and carefully leveled to a uniform thickness of 5 mm. The high-definition camera was used to capture the morphology of the silt surface. Three identical samples were tested simultaneously to assess the variability of the results.

SLOPE/W modeling of an embankment slope treated by MICP. A preliminary study was performed to investigate the effect of MICP treatment on improving the slope stability of an embankment slope model. SLOPE/W modeling was conducted using the geometry of the embankment slope reported by Stark, Ricciardi and Sisk (*14*) and soil properties of the silt measured in the direct shear tests. The results of the direct shear tests on MICP-treated samples were used to provide the improved soil parameters for MICP treated embankment slope model.

3. LITERATURE REVIEW

3.1. MICP Treatment

Ground improvement techniques are widely used in the field to fulfill the construction criteria. Compared to traditional techniques such as vibro-compaction and grouting, bio-cementation for ground improvement has been attracting increased research interest in the last decade. Bio-cementation increases soil shear strength by generating particle-binding materials (e.g., $CaCO_3$) through microbial processes ([15]).

One primary bio-cementation technique is microbially induced carbonate precipitation (MICP), which utilizes urea hydrolysis to increase the pore fluid's alkalinity and induce calcium carbonate precipitation ([16]). Realizing Microbial Induced Carbonate Precipitation (MICP) using urea hydrolysis bacteria *Sporosarcina pasteurii* (S. Pasteurii, ATCC 11859) is the most widely researched process. *S. Pasteurii* (ATCC 11859), an alkalophilic soil bacterium with a highly active urease enzyme, decomposes urea into ammonium (NH^{4+}), bicarbonate (HCO_3^-), and hydroxide ions (OH^-) and creates an alkaline environment (pH>7). This alkaline environment shifts the chemical equilibrium of carbon dioxide to supersaturated carbonate, which is required for the precipitation of calcium carbonate ($CaCO_3$). Calcium carbonate is nucleated on bacteria cell surface containing immobilized calcium (Ca^{2+}) ion and forms calcite or vaterite (determined by urease activity). Simultaneously, the negatively charged bacterial cell may attach to the soil particle surface due to the interaction between attractive London-van der Waals force and the repulsive electrostatic force between sand and bacteria surfaces. During this process, the growth of $CaCO_3$ will bridge between soil particles and create a bond, enhancing the strength and stiffness of the soil matrix are enhanced.

MICP can significantly improve the engineering properties of sands. Harkes et al. ([17]) injected S. pasteurii into a column of sandy soil and measured the unconfined compression strength (UCS) ranging from 0.2 to 20 MPa with 30 to 600 kg/m^3 calcium carbonate precipitation. Van Paassen ([18]) performed MICP treatment on sand samples and reported UCS ranging from 1 to 12 MPa with calcium carbonate content ranging from 0 to 24% by weight. DeJong, Fritzges and Nüsslein ([5]) injected S. pasteurii into a sand column for MICP treatment and reported that the shear stress ratio increased from 1.0 to 3.5 compared to untreated sand at 1% axial strain. During MICP treatment, the precipitated $CaCO_3$ which deposited around particles and occupied pore space reduces the permeability of the soil matrix. The highest permeability reduction was obtained in Al Qabany and Soga ([9]), showing a maximum decrease of approximately 99%. The permeability of fine and coarse sands of Cheng, Cord-Ruwisch and Shahin ([19]) showed a slower reduction with the maximum reduction of 80%. This wide variation of permeability reduction versus $CaCO_3$ content could be attributed to the differences of sand types, relative densities, concentrations of urea and $CaCl_2$, and test conditions ([9]).

The physical behavior of soil treated by MICP is controlled by the physical properties and distribution of $CaCO_3$ at particle-scale. Several morphologies of $CaCO_3$ were observed in the MICP-treated sand matrix, including spherical vaterite and cubic calcite. Different morphologies are controlled mainly by the hydrolysis rate of urea and $CaCO_3$ precipitation rate. However, the effects of different morphologies on the soil behavior were not reported, which were assumed to have similar effects between different morphologies. Rebata-Landa ([20])summarized the effect of MICP on soil properties at particle-scale. As $CaCO_3$ content increases, the stiffness, strength, and

dilatancy of MICP-treated soil increase while the hydraulic conductivity decreases. In addition, different types of $CaCO_3$ distributions at pore-scale will affect the soil physical behavior differently. For example, Yun and Santamarina (*21*) reported that cementing materials developed at particle contacts has maximum influence on granular mechanical response.

Most studies investigated the mechanical properties of sands treated by MICP and their geotechnical applications in sandy soils (e.g., liquefaction mitigation, stabilizing coastal sand dunes and fugitive dust, and improving pile capacities by bio-grouting) (*4; 5; 8; 22-27*). However, limited studies have been conducted on MICP-treated fine-grained soils (*28-30*). This is because the small pore-throat size among fine-grained soil restrains bacterial transport (*8*), which will be further investigated in this study.. Furthermore, most MICP studies are limited to laboratory-scale tests. Field-scale applications involve the in-situ injection of bacteria and cementation solutions, which could encounter significant heterogeneous treatment and is probably not applicable for fine-grained soil.

Since the pore size of fine-grained soils is significantly smaller than sandy soils, bacteria transport and colonization in fine-grained soils encounter difficulties (*9; 31*). The percolation and injection of MICP treatment solutions used in sandy soils may not apply to fine-grained soils due to their low permeability (*29*). Thus, different MICP treatment methods for fine-grained soils were investigated, such as kneading and mixing (i.e., thin-layer by thin-layer mixing of soil and MICP solutions) (*29*), mixing and pressure-injection (i.e., mixing soil with a medium containing the bacteria suspension and then injecting the cementation medium under pressure) (*28; 32*), bioencapsulation (i.e., forming $CaCO_3$ precipitation shells around clay balls) (*29*), and injection of crude urease obtained from the lysis of ureolytic bacteria into soil (*33*). Sharma and Ramkrishnan (*34)* applied MICP treatment to two types of clays (i.e., intermediate compressible clay and highly compressible clay). Their results show that both clays obtained considerable improvement in the UCS with 1.5 to 2.9 times increments. Also, the amount of the strength increment was proportional to the duration of the MICP treatment. Won et al. (*35*) investigated the effect of kaolinite on MICP treated sand samples. The results showed that the kaolinite particles worked as nucleation sites and facilitated the heterogeneous nucleation of calcium carbonate. Meanwhile, the well-predicted deposition profile of kaolinite correlated well with the deposited $CaCO_3$ profile. Li (*29)* conducted several feasibility studies on the MICP-treated kaolin, marine clay, and bentonite samples using unconfined compression, triaxial, oedometer, and direct simple shear tests. The experimental results showed that a higher shear strength was observed for all soil types treated by MICP as compared to untreated soils under the same water content. Soon et al. (*28*) explored the feasibility of using MICP for improving the engineering properties of a tropical residual soil (ML). The obtained shear strength increased by 69% and hydraulic conductivity reduced by 90%. Islam, Chittoori and Burbank (*30)* investigated the applicability of biostimulation (i.e., utilizing natural microbes existing in the clayey soils to precipitate calcium carbonate) to stabilize clayey soils. The clay samples were first injected with 1 pore volume of the enrichment solution to stimulate the growth of bacteria. Then, 1 pore volume of the cementation solution was injected to precipitate calcium carbonate. The unconfined compressive strength (UCS) increased in all clayey soil samples after MICP treatment. The increase in strength was attributed to the formation of calcium carbonate in the soil matrix. However, the possible biogeochemical reactions in the fine-grained soils during MICP treatment (e.g., the soil minerals may react with MICP solutions due to the increasing pH and the presence of carbonate ions) is not fully investigated (*36*), which will be further investigated in this study.

3.2. Soil Cracks and Embankment Slope Stability

Highway embankment slope failures result in road closures, damage public and private property, and cause serious safety hazards. Restoring highway embankment slope failures is a major challenge with considerable impacts on State and Federal maintenance budgets. Highway slope failures are ubiquitous across Region 6.

Most of these slope failures happened due to desiccation cracks induced by wetting and drying weather cycles. Desiccation cracking can degrade the mechanical and hydraulic properties of soil. The formation of the desiccation cracks allows water infiltration into the embankment, increasing the moisture content and reducing the shear strength of soils, and eventually causing embankment slope failures. Wang, Li and Zhang (*37)* explored the influence of cracks on the stability of embankment slopes subjected to rainfall infiltration. Commercial software, SEEP/W and SLOPE/W, were used for slope stability analysis for the saturated-unsaturated cracked soil slopes. Results showed that the pore water pressure distributions in the slope and the factor of safety of the slopes are affected by the presence of soil cracks. When the crack is shallow, the pore water pressure profile and factor of safety experienced small changes. However, when deep cracks exist, pore water pressures increase significantly and the factor of safety of the slopes decreases rapidly.

Slope repair approaches have been used to restore the embankment slopes such as using geosynthetics, soil nails, retaining structures, plastic pins, surface water management, lime, and vegetation, etc. For example, in Louisiana, most highway embankments with slope failures were repaired using Nonwoven geotextiles placed at a 12-inch vertical spacing to provide a form of reinforcement. Using vegetation in combination with mechanical reinforcement such as geogrids and geotextiles is also used. Vegetation on slopes also prevents surface erosion and shallow sliding (*38; 39*). Vegetation roots aggregate soil particles and provide cohesion that improves stability against shallow sliding. Furthermore, plant roots could reduce pore pressures in slopes by reducing infiltration and by evapotranspiration. However, vegetation is not effective for remediating deep slope failures.

Drainage is the most frequently used method for stabilizing slopes (*40*). The drainage could help lower groundwater level and reduce pore pressures, which will increase the factor of safety of the slopes. Drainage improves slope stability using two mechanisms: (1) It reduces pore pressures and increases effective stress and shear strength; and (2) it reduces the driving forces of water pressures in soil cracks and reduces the shear stress required for equilibrium. Several methods in drainage could be used to stabilize slopes, including surface drainage, horizontal drains, drain wells and stone columns, wellpoints and deep well, trench drains, drainage galleries and counterfort drains (*40*).

Retaining structures can be used to improve slope stability, including prestressed anchors and anchored walls, gravity walls, MSE walls, and soil nailed walls (*40*). These retaining structures can provide stabilizing forces to slopes, thereby reducing the shear stresses on potential slip surfaces. Prestressed anchors and anchored walls require bearing pads to distribute their loads to the surface of the slope. Soldier piles are usually driven into the soil and wood lagging is then fitted between the flanges of the soldier piles. The anchors are then installed. The anchored walls can be evaluated using the conventional limit equilibrium slope stability analyses. The force applied by the anchors needs to be included in the limit equilibrium slope stability analyses, acting

at a known location on the slope. The anchor force should be a working load (i.e., the ultimate anchor capacity divided by a suitable factor of safety). Conventional gravity retaining walls, mechanically stabilized earth (MSE) walls, and soil nailed walls, can also stabilize slopes. The design of these retaining walls can be designed using three steps: (1) determining the force required at the location of the wall to stabilize the slope using conventional limit equilibrium slope stability analyses, (2) determining the external dimensions of the retaining wall, MSE wall, or soil nailed wall using conventional retaining wall design procedures, and (3) evaluating the requirements for internal strength using conventional design procedures. The requirements for internal strength include the shear and moment capacity of the footing and stem (for gravity walls), the length of reinforcement, the strength of reinforcement, and spacing of reinforcement (for MSE walls), and nail capacity, nail length, and nail spacing (soil nailed walls).

Injection methods, including lime piles and cement grout, are also used to stabilize slopes (*41*). However, the disadvantage of these methods is that they are difficult to quantify the beneficial effects. Also, when grout fluids are injected, the slope could be less stable in the short term. The beneficial effects may be achieved when the injected grout has hardened. Lime piles are drilled holes filled with lime. Lime piles can react with and strengthen the fill soils, which can reduce slide movement. Injecting cement grout has also been used extensively to stabilize landslides. The grouting pressures are ranged between 20 and 75 psi. Cement grout could be used to stabilize landslides in clay. However, cement cannot penetrate clay because the cement particles are larger than the voids of clays. Based on field experiments, the grout can penetrate along the rupture surface in clay and lift the soil mass above, resulting in a solid mass of neat cement concrete forming along the slip surface (*42*). Cement was also used in crack healing. Arya, Wiraga and Suryanegara *(43)* performed several lab-scale slope stability tests using Portland cement. Cement can create bonds between soil particles, which will stiffen the slope against failure. The first model was the slope without cement. The second model was a slope treated by cement injection. The results showed that the shear strength of the soil treated by cement increased from 32º to 48º. The increased amount of internal friction angle has increased the factor of safety from 0.78 (untreated) to 1.17 (after cement treatment).

In addition, removing and replacing the sliding mass needs to be performed when a sliding mass has moved a long distance and has become disturbed and softer as a result of the movement. Excavation is not undertaken until the sliding stability has increased (e.g., by drainage). When excavating the sliding mass, it is important to excavate below the rupture surface into the undisturbed soil to remove all the unstable material. Then, the slope is reconstructed. However, most of the above methods involve large earth work, special installation equipment, and special construction processes, which may delay the construction timeline, cause road closure, and increase the project cost.

Microbially induced calcite precipitation (MICP) has arisen as a green and sustainable soil improvement technique, which may provide an efficient way of crack remediation. Vail et al. *(44)* used a series of cyclic wetting-drying tests and showed that MICP significantly delayed the initiation of desiccation cracks in the high plasticity clay (bentonite). Both surface cracking ratio and average crack width were less than the untreated groups. Wang et al. *(3)* conducted laboratory experiments and finite element modeling to investigate MICP-treated sand slope failure under rainfall conditions. They concluded that MICP treatment groups significantly improved the erosion resistance and the stability of the embankment slope.

4. METHODOLOGY

4.1. Direct Shear Tests on MICP-Treated Silt

4.1.1. Materials

4.1.1.1. Bacteria Cultivation and MICP Treatment

Table 1 presents the solutions used for growing the bacteria cells (e.g., tris buffer and growth medium) and for MICP treatment (i.e., urea medium and cementation medium). The gram-positive bacteria Sporosarcina pasteurii strain ATCC 11859 (obtained from American Type Culture Collection, ATCC) was used in this study. The frozen stocks of the bacteria were prepared according to Lin et al. (*24*). To prepare bacteria cells for MICP treatment, bacteria from frozen stocks were cultivated in the growth medium (Table 1) inside a shaking incubator at 30°C for about 24 hours. The bacteria cells were then harvested at OD_{600} = 0.8~1.2 (OD_{600}: optical density of a sample measured at a wavelength of 600 nm), centrifuged at 5000 rpm for 20 min (Refrigerated centrifuge for 3 L centrifugation) and 4000 rpm for 30 min (benchtop centrifuge for 200 mL centrifugation) to a targeted bacteria density of 1×10^8 cells/mL (*24*). The bacteria cells were then stored in the 4°C fridge (two weeks maximum) before use. The MICP treatment media, including urea medium and cementation medium, are also shown in Table 1. Urea medium was used for urea hydrolysis by bacteria cells. The cementation medium was used to induce $CaCO_3$ precipitation in the soil matrix.

Table 1. Summary of media employed to grow cells and conduct microbially induced carbonate precipitation (MICP).

Solution	Constituents
Tris Buffer	7.6 g Tris hydrochloric acid 54.7 g Tris base in 500 mL deionized water
Growth Medium[#]	20 g Yeast extract 10 g Ammonium sulfate In 1 L of 0.13 M Tris buffer (pH = 9), sterilized by filter
Urea Medium	20 g/L Urea 2.12 g/L $NaHCO_3$ 20 g/L NH_4Cl 3 g/L Bacto nutrient broth Adjust pH to 5.5 with 5 M HCl sterilized by filter
Cementation Medium	Same as Urea Medium but additionally supplemented with 147g/L $CaCl_2 \cdot 2H_2O$

[#]The growth medium is the ATCC medium 1376 that is recommended for growing the bacteria strain.

4.1.1.2. Soil Type and Properties

The soil was collected near the Accelerated Loading Facility of the Louisiana Department of Transportation and Development (LA DOTD). According to the unified soil classification system (USCS), the soil is classified as low-plasticity silt with some sand and clay (ML). The grain size distribution is analyzed using sieve analysis and PARIO hydrometer test (Meter Company, Pullman, WA), which is shown in Figure 1. The liquid and plastic limits are 33% and 26%, respectively. The optimum moisture content and the maximum dry unit weight are 9.7% and 14.7 kN/m^3, respectively. Based on the XRD analysis, the silt consists of quartz, albite, muscovite, and glauconite. Albite is a feldspar mineral. Muscovite is a mica mineral. Both albite and muscovite are nonclay minerals. Glauconite is an iron-rich illite mineral, which is the most commonly found clay mineral in soils (*45*).
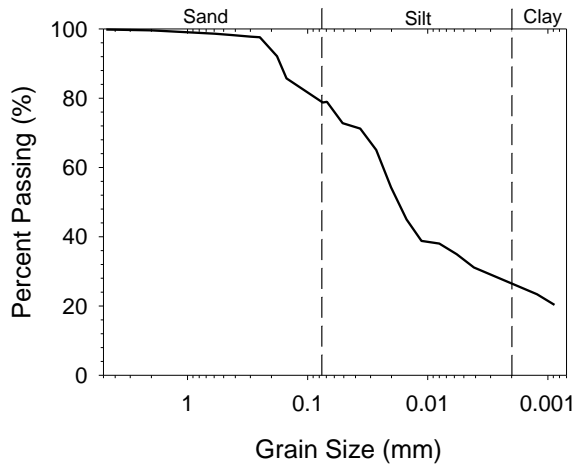
Figure 1. Particle size distribution of the silt.

The soil was also classified using the revised soil classification system (RSCS) (*46; 47*). Compared to the USCS, RSCS can better capture the fines threshold fractions that begin to control the mechanical and hydraulic properties of the soil matrix and can reflect the role of pore-fluid chemistry (i.e., different pore-fluids that have contrasting permittivity and electrical conductivity) in the behavior of fines (*47*). The input parameters for RSCS include the particle size distribution, uniformity coefficient (Cu), coarse grain roundness (R), and liquid limits of soil passing sieve No. 200 with different types of pore fluids. The sand grain roundness (R) was determined visually using an optical microscope (SWIFT Pro Digital Compound Microscope) by referencing the particle shape charts in Cho, Dodds and Santamarina (*48*). Fall cone tests using three types of pore fluids, including deionized water, kerosene (low permittivity), and 2M NaCl brine (high ionic concentration), were used to determine the liquid limits of soil passing sieve No. 200 following Jang and Santamarina (*46*). The liquid limits in deionized water, kerosene, and 2M NaCl brine are 42%, 37%, and 39%, respectively. The accompanying RSCS Excel sheet provided by Park and Santamarina (*47)* was used to classify the soil using RSCS. The classification charts are shown in Figures 2a and b. Figure 2s shows that the test soil has 79% of fines (passing sieve No. 200) and 21% of sand (between sieve Nos. 4 and 200). The soil is in the F(F) region, indicating that the fines fraction controls the mechanical properties and fluid flow of the soil matrix. Figure 2b shows that the soil has a low plasticity and a low electrical sensitivity to pore fluid chemistry (SE=0.13). The electrical sensitivity SE is defined to capture the changes in liquid limit with pore fluids that have different permittivity and electrical conductivity (e.g., deionized water, kerosene and 2M

NaCl brine). More information about the calculation of electrical sensitivity can be found from Jang and Santamarina (*46)*.

(a)

(b)
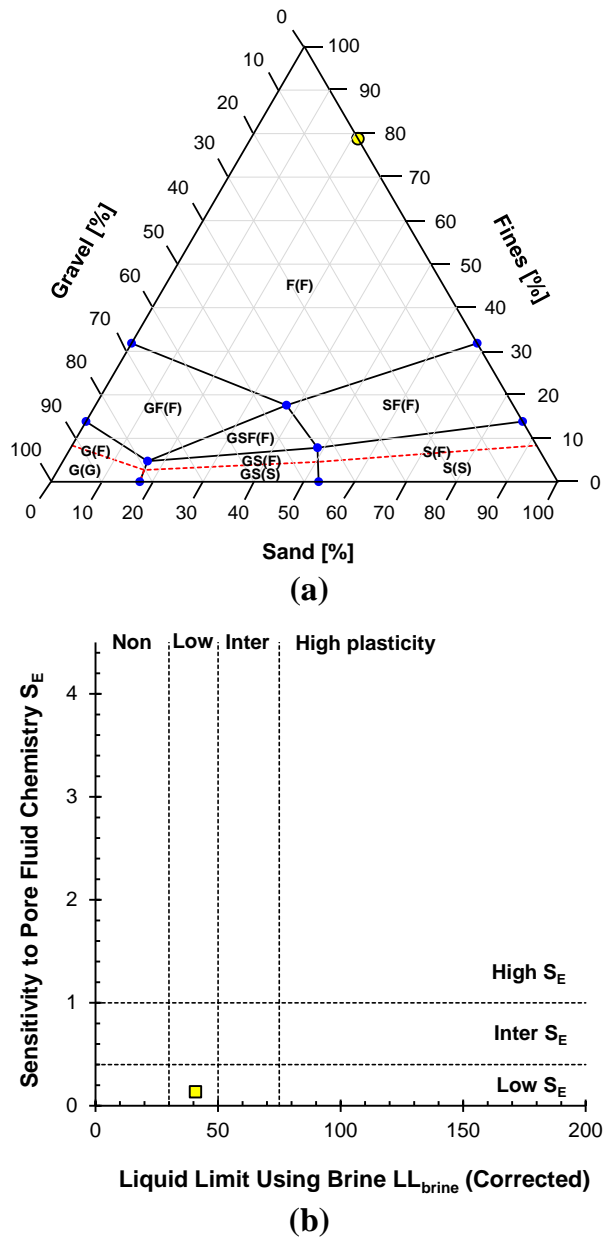
Figure 2. Revised soil classification system (RSCS) results: (a) soil-specific triangular chart and (b) fines classification chart.

4.1.2. Experimental Procedures

4.1.2.1. Test Types

Three types of direct shear tests were performed in this study using three different treatment solutions, including (1) deionized water (named untreated), (2) urea medium suspended with

bacteria cells (named UB), and (3) urea medium, bacteria cells, and cementation medium (named UBC) as shown in Table 2. Also, three different confining pressures were used to investigate the effect of confining pressures on soil behavior (Table 2). Three types of treatment solutions used the same volume (total of 30 mL as shown in Table 2) and same density of bacteria cells (i.e., 1×10^8 cells/mL). Untreated tests were served as control by adding 30 mL of deionized water to investigate the mechanical behavior of the silt without MICP treatment. The UB treatment includes a urea medium (30 mL) mixed with bacteria, which was used to investigate the mechanical behavior of the UB-treated silt samples without adding cementation medium (i.e., without adding calcium chloride). The UBC treatment has been widely used for MICP treatment in the literature, including urea medium (10 mL), bacteria cells, and cementation medium (20 mL). It is important to note that all tests were successfully duplicated to verify repeatability and validate the results.

Table 2. Test types of direct shear tests.

Test Type	Confining Pressure (kPa)	Urea Medium Volume (mL)	Cementation Medium Volume (mL)	Deionized Water Volume (mL)
Untreated	12	0	0	30
Untreated	25	0	0	30
Untreated	35	0	0	30
UB	12	30	0	0
UB	25	30	0	0
UB	35	30	0	0
UBC	12	10	20	0
UBC	25	10	20	0
UBC	35	10	20	0

Note: Untreated tests used deionized water only; UB tests used urea medium and bacteria cells; UBC tests used urea medium, bacteria cells, and cementation medium.

4.1.2.2. Sample Preparation and MICP Treatment Procedures

Since the soil failure surface in the direct shear tests is located at the shear interface between the direct shear split boxes, we designed a MICP treatment procedure to target for treating the soil at the shear interface that controls the mechanical behavior of the direct shear samples. Vacuum grease (Dow Silicones Corporation) was used to seal the small gap between the top and bottom split boxes to prevent leakage of the MICP treatment solutions and to reduce the friction resistance between the two shear boxes. The silt was first dried in an oven at 100°C for 24 hours. After drying, the silt was mixed with deionized water to achieve the optimum water content of 9.7%. The mixture was then sealed and equilibrated for 18 hours. After homogenization, the silt was first compacted to fill the bottom split box (Figure 3a), followed by filling 30 mL of the MICP solutions (for UB-and UBC-treated samples) or deionized water (for untreated samples) into the split box (Figures 3b and c). Stored bacteria cells were suspended in the targeted volumes (10 or 30 mL) of urea medium (Table 1), stirred, and introduced into the direct shear box (Figure 3b). Then, the targeted volume (20 mL) of cementation medium (Table 1) for UBC-treated samples was introduced into the direct shear box (Figure 3c). Immediately after the inoculation of the treatment

solutions, additional silt was compacted into the top split box to achieve the dry density of 14.7 kN/m³ (Figure 3d). The final size of the direct shear test samples was 63.5 mm in diameter and 31.8 mm in depth. Porous stones and filter papers were installed at the top and bottom of the silt samples for water drainage and soil retention.
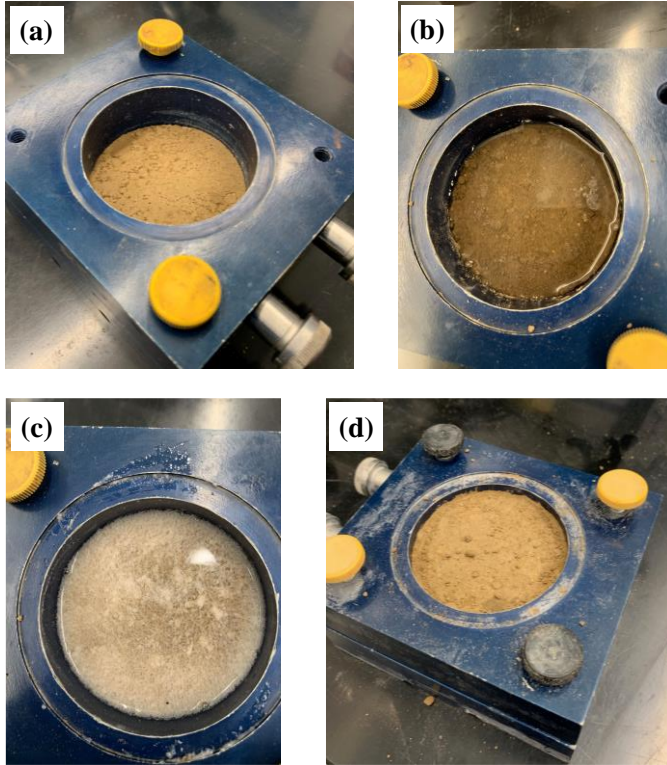
Figure 3. Direct shear sample preparation: (a) compacted silt in the bottom split box, (b) urea medium suspended with bacteria cells or deionized water filled in the split box, (c) cementation medium added into the split box, and (d) compacted silt added into the top split box.

4.1.2.3. Direct Shear Tests

The Geotac Automated Direct Shear System was used to investigate the mechanical behavior of UB-and UBC-treated and untreated silt samples. The direct shear tests were performed following the ASTM standard D3080 (*49*). After sample preparation and MICP treatment, the samples were saturated with water. The samples were then subjected to consolidation for 24 hours under three consolidation pressures (12, 25, and 35 kPa, Table 2). After consolidation, direct shear tests were performed using a displacement rate of 0.032 mm/min to achieve a consolidated drained test condition.

4.1.2.4. Equivalent CaCO3 Content Measurements

After the direct shear tests, three specimens were collected from each direct shear sample at the depths of 11, 17 (at the shear interface), and 23.5 mm and were then oven-dried for $CaCO_3$ content measurements (defined as the mass of $CaCO_3$ divided by the mass of dry soil without $CaCO_3$). The $CaCO_3$ contents of the specimens were quantified in accordance with the ASTM standard D4373 (*50*). Silt specimens (about 25 g) were placed in a sealed test chamber and reacted with hydrochloric acid (1M, 30 mL) to generate carbon dioxide gas. The generated carbon dioxide gas could increase the air pressure in the test chamber, which was monitored by a pressure gauge. The

final readings (air pressure in kPa) of the pressure gauge were recorded after 2 hours of the reaction. The relationship between pressure reading and mass of $CaCO_3$ was calibrated by measuring the corresponding pressure reading under the defined mass of $CaCO_3$ (0, 0.2, 0.4, 0.6, 0.8, and 1 g, reagent grade). The calibrated relationship between the pressure readings and $CaCO_3$ masses was used to determine the $CaCO_3$ contents of the silt specimens from the measured pressure readings.

It is important to note that soil minerals may react with MICP media due to increasing pH and the presence of carbonate ions (*15; 51*). Thus, other precipitation compounds (e.g., iron carbonate) could be produced during MICP treatment. This means that the $CaCO_3$ content measurements in this study are, in fact, equivalent $CaCO_3$ contents of the silt samples. The original equivalent $CaCO_3$ content of the untreated silt was first measured (about 2%), which serves as a baseline. The equivalent $CaCO_3$ contents of the UB-and UBC-treated samples were calculated by subtracting the baseline equivalent $CaCO_3$ content (2%) from the measured $CaCO_3$ contents.

4.1.2.5. SEM, EDS, XRD, and Raman Spectroscopy

After direct shear tests, additional specimens were collected from the shear interface of the direct shear samples for SEM imaging, EDS, XRD, and Raman spectroscopy analysis. The Quanta 3D Dual Beam SEM was used for investigating the morphology and structure of the silt specimens. The EDS system was integral to the SEM device and was used to analyze the elemental compositions of the specimens and to conduct calcium cation mapping on the specimens. The mineral compositions of the soil specimens were characterized by a Panalytical Empyrean X-ray diffractometer (XRD). The XRD scans were recorded with a Cu Kα radiation (λ=1.54 Å, 45 kV, and 40 mA) in the 2θ range from 5° to 80° with a scan rate of 4°/min. In addition, Renishaw inVia Reflex Raman microscope/spectroscope was utilized to identify the chemical signatures of changes in the silt specimens before and after the MICP treatments. The 633 nm laser was chosen as the excitation source for the measurements on the silt samples. The Raman spectrum was carried out using the synchro mode from 200 to 3000 cm^{-1} with an exposure time for each scan of 10 s. All the spectra were obtained at a 20X magnification. Before the Raman scanning tests, calibrations were done using a 520.5 cm^{-1} line of a silicon wafer.

4.2. Wetting and Drying Cycle Tests

4.2.1. Soils and MICP Recipe

The silt used in the direct shear tests was used in this study. The MICP treatment solutions were the same as those used in the direct shear tests.

4.2.2. Sample Preparation

The silt was air-dried for 24 hours and passed through sieve No. 16 (opening size=1.18 mm). The passing silt was then mixed with deionized water to achieve a water content at liquid limit (around 42% water content). After homogenization, the silt was poured into the 150-mm diameter Petri dishes, lightly compacted, and carefully leveled to a uniform thickness of 5 mm as shown in Figure 4. Three similar samples were tested simultaneously to check the variability of the results.

Figure 4. Setup of the cyclic wetting and drying tests.

4.2.3. Testing Procedure

Three similar samples were prepared and tested using the same procedure. Three silt samples were subjected to two initial wetting-drying cycles (denoted as Treatments 0 and 1) and two subsequent wetting-drying cycles (denoted as Treatments 2 and 3). Each cycle lasted about 96 hours and contained two stages, including the drying stage followed by the wetting stage. In the drying stage, samples were exposed to thermal heating using two light bulbs for 48 hours. The soil surface temperature was measured by a thermal gun (ETEKCITY lasergrip 774). The soil surface temperature was constant at $60\pm1°C$. In the wetting stage, the light bulbs were turned off and the temperature was cooled down to $20 \pm 1°C$ (lab temperature, checked by the thermal gun). Deionized water was dribbled to the surface of the silt samples using the 5mL syringe until the total sample weight returned to the original sample weight (i.e., the weight before the first wetting-and-drying treatment) followed by a retention time of 48 hours. To apply MICP treatment, MICP treatment media were applied on the samples instead of deionized water for the wetting stage of Treatment 2. The bacteria cells and urea medium (9 mL) were dribbled into the cracks of samples using 5mL syringes, followed by cementation medium (9 mL). After each treatment cycle, the crack patterns of each sample were captured by a high-resolution camera mounted above the Petri dishes for image-based quantitative analysis.

To quantitatively compare the effects of the MICP treatment on the desiccation cracks of silt samples at different wetting-drying cycles, MATLAB and ImageJ software were used in this study. Figure 5 shows the processing procedure of a silt sample. Photos captured in different treatment cycles were first transformed into 8-bit binary figures in MATLAB with the same grayscale (Figure 5a). The binary figure was trimmed to remove the boundary of the Petri dish (Figure 5b) and then imported into ImageJ. In ImageJ, the figure was defined with the correct scale (Figure 5c). According to the definition of the crack length defined by Liu et al. (*52*), the crack length in this study is defined as the distance between two adjacent intersection nodes, as shown in Figure 5d. Also, the crack length of those cracks without intersections was defined as the distance between two "Node_0". The size of the "Node_0" should have three pixels that have the same color and

grayscale (adjusted through palette in Adobe Photoshop). Freehand lines were drawn in the binary figures to represent the crack lengths under 800x magnification (Figure 5e). In order to calculate the total crack area of a sample, several freehand curves were drawn to cover a single crack area, under 800x magnification (Figure 5f). Following the similar procedures as shown in Figure 5f, other crack areas were found. The summation of all single crack areas was equal to the total crack area of the sample. The labelled crack areas are displayed in Figure 5g. In Figure 5g, the inverted colors between the cracks and soil sample were for illustration with a better contrast. The summation of the white area (intact soil surface) and the crack area (black area) was equal to the area of the Petri dish. The averaged crack width was then calculated by dividing the total crack area by the total crack length. The crack area percentage was calculated by dividing the crack area (black area as shown in Figure 5g) by the total area of the Petri dish (white and black areas together in Figure 5g).

Thus, the following parameters of the crack patterns were determined: (1) statistical data of crack length (determined by ImageJ), (2) total crack area (determined by ImageJ), (3) averaged crack width (total crack area divided by the total crack length); (4) crack area percentage (total crack area divided by the total sample surface area). The measurements of the cracking depths were not performed because the camera can only capture the two-dimensional information of the surface cracks.
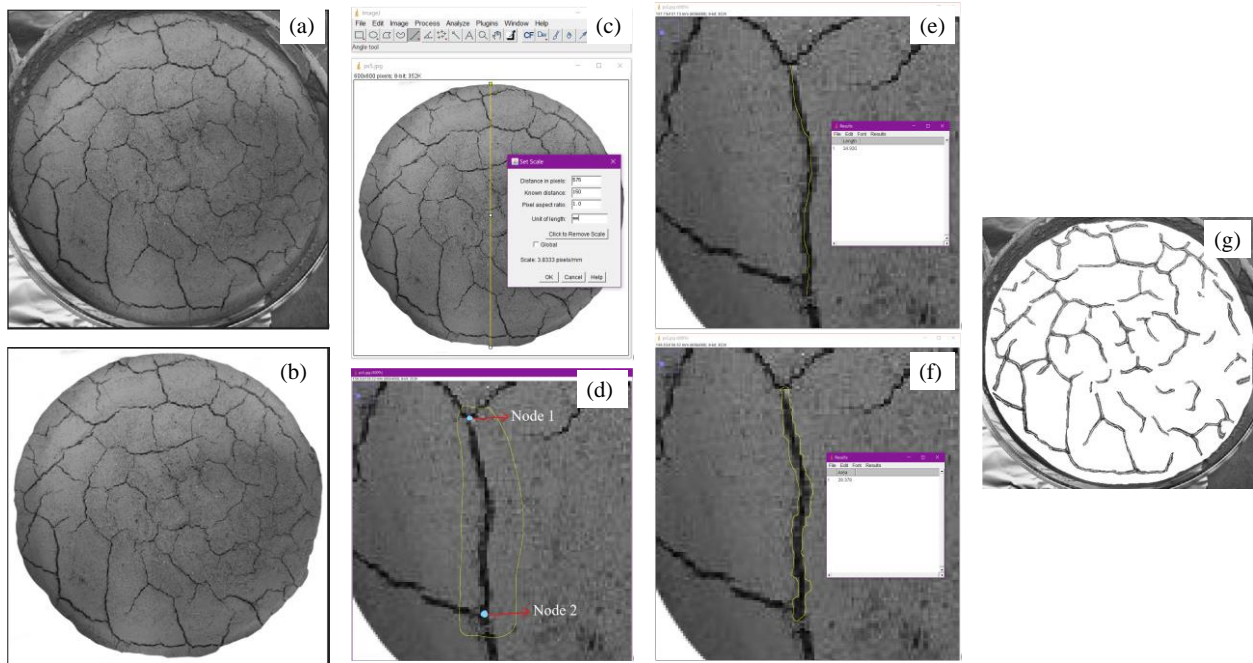
Figure 5. Image processing: (a) binary photo processed by MATLAB, (b) boundary of the Petri dish was removed, (c) define the scale of the photo, (d) define a crack length, (e) draw a curve to represent the crack length, (f) define a crack area, and (g) mark all crack areas and calculate the total crack area.

4.3. Preliminary Slope Stability Modeling

4.3.1. Parameters and Methods

Three SLOPE/W models were prepared under different treatment conditions. The untreated slope served as the control. Two types of MICP treatments were used to treat the slope models and

investigate their stabilities, including UB-treated and UBC-treated models. The soil properties measured from direct shear tests were used for each of the three models as shown in Table 3. In the untreated slope model, the cohesion and friction angle of the silt are equal to 5.9 kPa and 28.8°. The cohesion and friction angle of the silt in the UB-treated slope are 5.4 kPa and 33.9°. The cohesion and friction angle of the silt in the UBC-treated slope are 7.1 kPa and 37.6°. Figure 6 shows the slope geometry defined in the SLOPE/W. Soil properties in the SLOPE/W model have the same soil properties as the low-plasticity silt in Table 3. The slope stability analysis was performed using the Morgenstern and Price (*53*) method under drained condition. The blue dashed line is the defined groundwater table. The red solid lines represent the slip surfaces (Point 8 to 9 is the entrance slip surface and Point 5 to 6 is the exit slip surface).

Table 3. SLOPE/W input parameters.

Treatment Types	Unit Weight (kN/m³)	Cohesion (kPa)	Friction Angle (°)
Untreated	14.7	5.9	28.8
UB-treated	14.7	5.4	33.9
UBC-treated	14.7	7.1	37.6
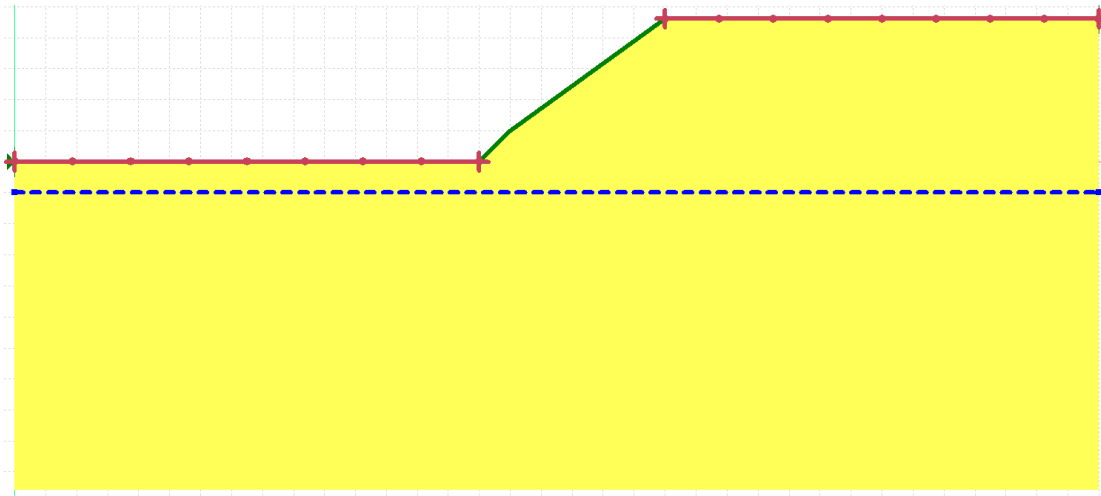
Figure 6. Geometry of the embankment slope in SLOPE/W.

5. ANALYSIS AND FINDINGS

5.1. Direct Shear Tests on MICP-Treated Silt

5.1.1. Shear Stress versus Horizontal Displacement

The relationships between shear stress and horizontal displacement of the silt samples under 12 kPa confining pressure (Figure 7a) show strain-softening behavior due to relatively low confining pressure. However, the shear stresses versus horizontal displacements of the silt samples under 25 and 35 kPa confining pressures reveal strain hardening behavior (Figure 8a and 9a). A comparison of untreated, UB-treated, and UBC-treated samples indicates that the peak shear strengths increased by an average of 12% for the UB-treated samples and 30% for the UBC-treated samples compared to the peak shear strengths of the untreated samples. When compared to the ultimate shear stresses of the untreated samples (defined as the shear stress at the horizontal displacement of 15 mm in this study), the ultimate shear stresses increased by an average of 30% for the UB-treated samples and 55% for the UBC-treated samples. The initial slopes between the shear stress and horizontal displacement were also calculated. As compared to the untreated samples, the initial slopes increased by an average of 24% for UB-treated samples and 80% for UBC-treated samples.

(a)

(b)
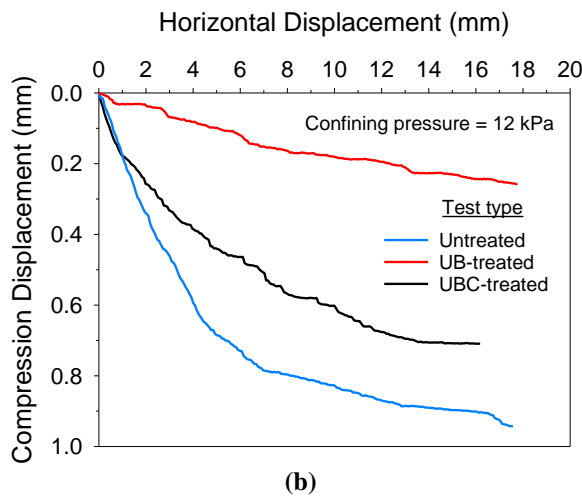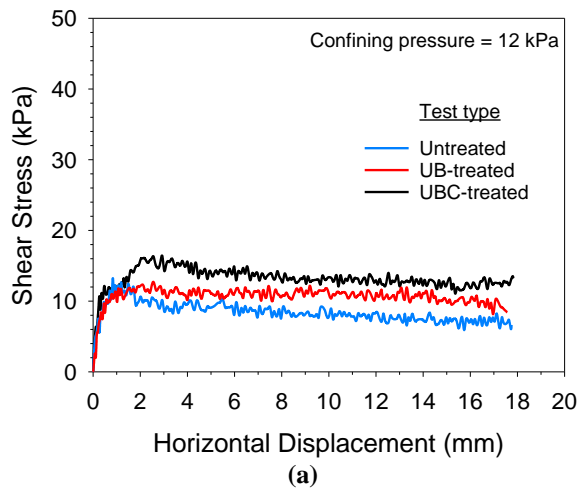
Figure 7. Direct shear test results of the silt samples at the confining pressure of 12 kPa: (a) shear stress versus horizontal displacement and (b) compression displacement versus horizontal displacement.

(a)

(b)
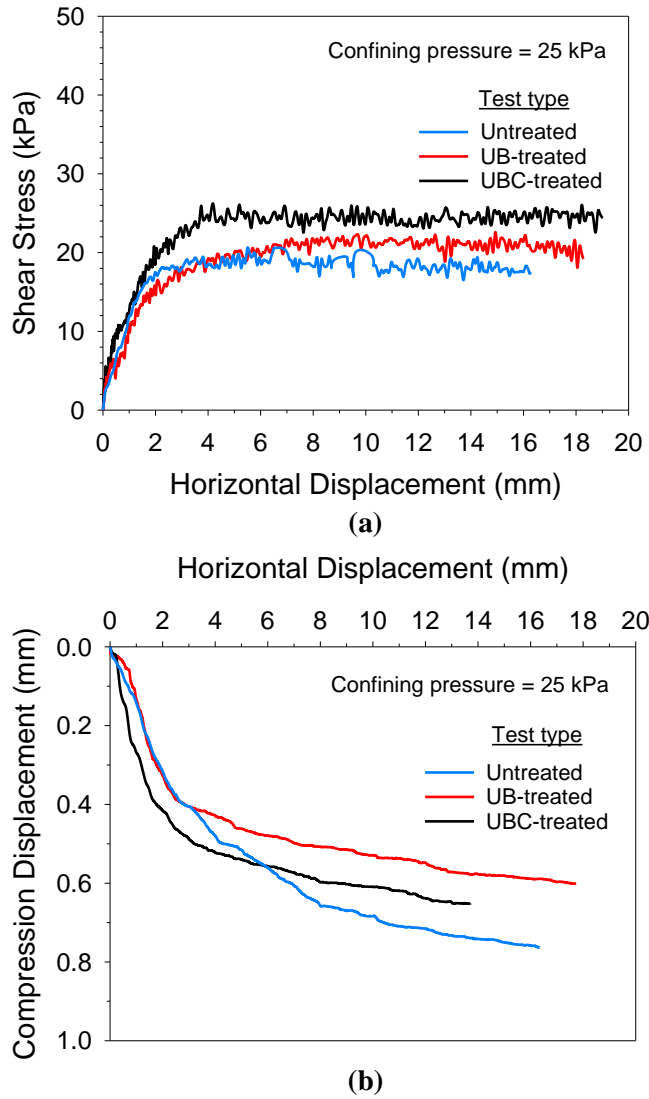
Figure 8. Direct shear test results of the silt samples at the confining pressure of 25 kPa: (a) shear stress versus horizontal displacement and (b) compression displacement versus horizontal displacement.
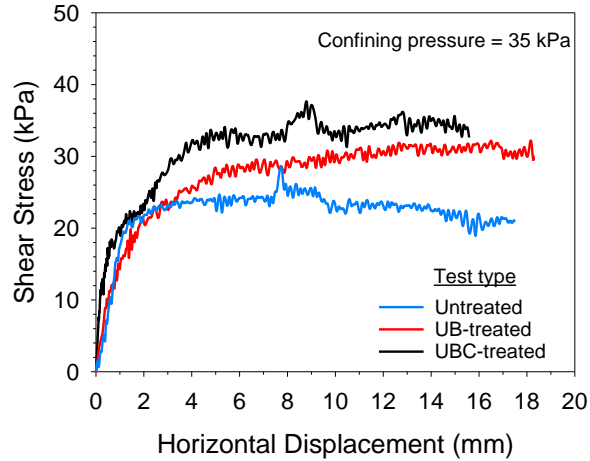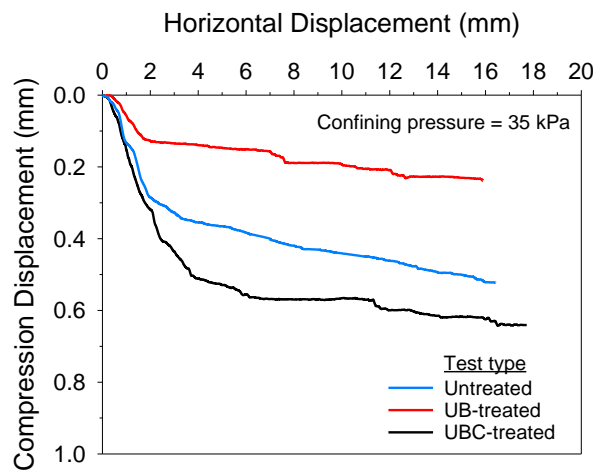
Figure 9. Direct shear test results of the silt samples at the confining pressure of 35 kPa: (a) shear stress versus horizontal displacement and (b) compression displacement versus horizontal displacement.

These results demonstrate that the peak and ultimate shear strengths were improved by UB and UBC treatments. The improvements of the peak and ultimate shear strengths of the UB-and UBC-treated samples are mainly attributed to the carbonate precipitations (e.g., calcium carbonate and iron carbonate) at the shear interface, cementing the soil particles together. Higher equivalent $CaCO_3$ contents at the shear interface were achieved in the UBC-treated samples, leading to the highest shear strengths of the UBC-treated samples. For UB-treated samples, since cementation medium (i.e., calcium chloride) was not used, $CaCO_3$ precipitation should be minimal. It is indicated that other precipitation compounds were generated during the UB treatment. It is also important to note that the direct shear test treated by the urea medium only (i.e., without bacteria cells and cementation medium) was also conducted. While its relationship of the shear stress versus the horizontal displacement was similar to the untreated samples, showing that the urea medium can not improve the mechanical behavior of the silt samples.

5.1.2. Volumetric Behavior

Figures 7b, 8b, and 9b present the relationships of the compression displacement versus horizontal displacement for untreated, UB-and UBC-treated silt samples under 12, 25, and 35 kPa confining

pressures. Untreated samples showed the highest vertical compression displacements compared to the UB-and UBC-treated samples except for the untreated samples under the confining pressure of 35 kPa. UB and UBC treatments can be seen to reduce the vertical compression displacements of the treated samples. UB-treated samples generally showed less settlements as compared to the UBC-treated samples. The different compression displacements between untreated and UB-and UBC-treated samples are controlled by the equivalent $CaCO_3$ contents and their distributions in the samples.

5.1.3. Equivalent CaCO₃ Contents and Distributions

Figures 10a, b, and c present the measured equivalent $CaCO_3$ contents along with the sample depth for the UB-and UBC-treated samples. It is important to note that the reported equivalent $CaCO_3$ contents of the UB-and UBC-treated samples as shown in Figures 10 were calculated by subtracting the baseline $CaCO_3$ content of natural silt (2%) from the measured $CaCO_3$ contents. The y-axis represents the depth from the sample top (0 mm) to the sample bottom (31.8 mm). Soil specimens were collected at three different depths (11, 17, and 23.5 mm) for equivalent $CaCO_3$ content measurements in accordance with the ASTM standard D4373 (50). The equivalent $CaCO_3$ content distributions of the UB-treated samples under 12 and 35 kPa confining pressures show a gradient along the sample height. The highest equivalent $CaCO_3$ contents are near the bottom (0.7%) and near the top (0.7%) for 12 and 35 kPa confining pressures, respectively. However, the equivalent $CaCO_3$ content is the highest at the shear interface (0.2%) for the UB-treated sample at 25 kPa confining pressure. For the UBC-treated samples under different confining pressures, the equivalent $CaCO_3$ contents were the highest at the shear interface (sample depth = 17 mm). The equivalent $CaCO_3$ contents are 0.9%, 0.5%, and 0.8% at the shear interface at confining pressures of 12, 25, and 35 kPa, respectively. However, the equivalent $CaCO_3$ contents at the depths of 11 and 23.5 mm of the UBC-treated samples were around 0%.
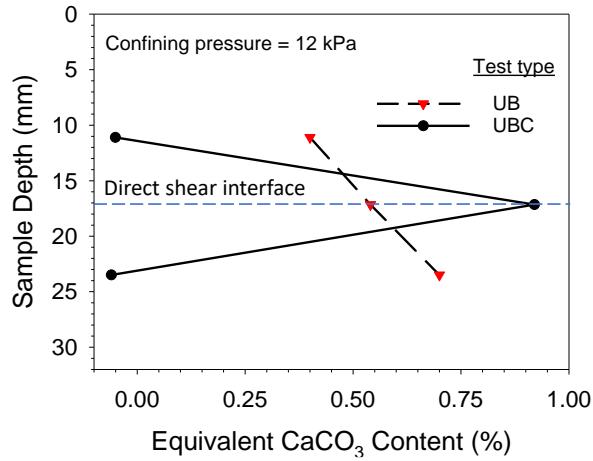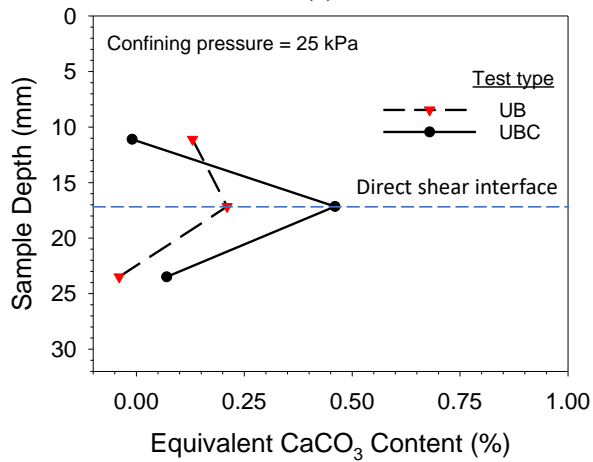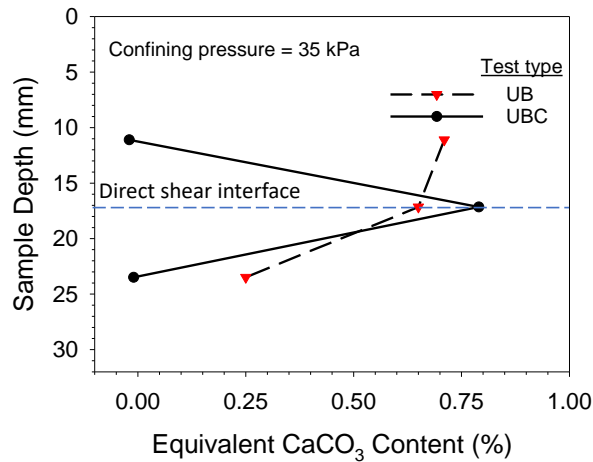
Figure 10. Equivalent CaCO₃ content distributions along the sample depth at confining pressures of: (a) 12 kPa, (b) 25 kPa, and (c) 35 kPa.

The highest equivalent CaCO$_3$ contents at the shear interface (i.e., depth of 17 mm) of the UBC-treated samples may be attributable to the fast ureolysis and CaCO$_3$ precipitation rates after adding cementation medium (i.e., adding CaCl$_2$ promoted fast precipitation of CaCO$_3$). In contrast, since

no cementation medium was added in the UB-treated samples, the precipitation rates of other carbonate compounds (e.g., iron carbonate) were lower than that of the UBC-treated samples. This means that the UB treatment solutions could permeate in the silt samples during sample preparation, which induced higher equivalent $CaCO_3$ contents at the sample top and bottom (i.e., at depths of 11 and 23.5 mm).

The relationships of the shear stress and horizontal displacement (Figures 7a, 8a, and 9a) are controlled by the equivalent $CaCO_3$ contents at the shear interface. It can be seen from Figures 10a, b, and c that the equivalent $CaCO_3$ contents at the shear interface of the UBC-treated samples ranged from 0.5% to 0.9%, which are an average of 70% higher than those of the UB-treated samples (ranged from 0.2% to 0.65%) under the same confining pressure. Therefore, the UBC-treated samples with higher equivalent $CaCO_3$ contents at the shear interface showed higher peak and ultimate shear strengths than those of UB-treated samples. Furthermore, the distributions of the equivalent $CaCO_3$ contents affected the measured compression displacements, as shown in Figures 7b, 8b, and 9b. Since the UB-treated samples showed larger distributions of the equivalent $CaCO_3$ contents as compared to the UBC-treated samples (equivalent $CaCO_3$ contents concentrated at the shear interface only), the compression displacements of the UB-treated samples were lower than the UBC-treated samples.

5.1.4. Failure Envelopes

The Mohr-Coulomb failure envelopes were produced using the direct shear test results. Figure 11 shows the peak failure envelopes of the untreated, UB-and UBC-treated samples. The friction angles and cohesions were calculated from the fitted failure envelopes. The peak friction angles of untreated, UB-treated, and UBC-treated samples are 28.8º, 33.9º, and 37.6º, respectively. The cohesions of the untreated, UB-treated, and UBC-treated samples are 5.9, 5.4, and 7.1 kPa, respectively. The increasing friction angles of untreated, UB-treated, and UBC-treated samples may be attributed to the precipitation of $CaCO_3$ and other precipitation minerals at the shear interface (Figure 10), which modified the frictional resistances of the soil matrix. The higher cohesion (7.1 kPa) of the UBC-treated samples is due to the higher equivalent $CaCO_3$ contents achieved at the shear interface than the UB-treated samples (Figure 10).
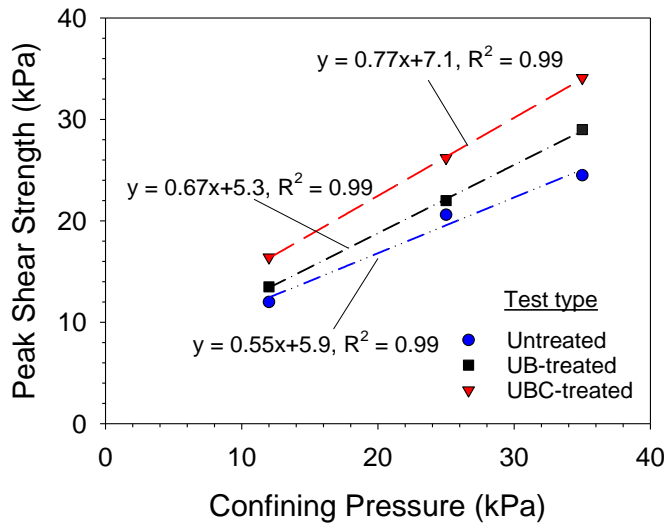
Figure 11. Peak failure envelopes of untreated, UB-treated, and UBC-treated samples.

5.1.5. SEM Imaging and EDS Analysis

The SEM imaging and EDS analysis on silt samples are shown in Figure 12. The comparisons of the SEM images (Figures 12a, b, and c) between different samples show that the untreated sample has better-defined particles, while the particles in the UB-and UBC-treated samples are not well defined, which is possibly attributed to the $CaCO_3$ and other minerals precipitation. It was reported that $CaCO_3$ precipitation could form cementation bonds and coating on soil particles during MICP treatment (*51; 54-56*). The elemental compositions of the untreated and UB-treated samples show the existence of calcium cation (0.8 and 1.8 %, respectively), indicating the existence of $CaCO_3$ in the natural silt. However, the calcium content of the UBC-treated sample is 4.7%, which is significantly higher than those of untreated and UB-treated samples. The calcium mapping (light green color shown in Figure 12d) from the EDS analysis demonstrates a large distribution of calcium element in the UBC-treated samples. This means that a large amount of $CaCO_3$ precipitation happened in the UBC-treated samples. In addition, EDS analyses show iron cation (5.1% to 9.9%) existing in the silt, which may lead to the precipitation of iron carbonate and iron hydroxide during MICP treatment.

Element	Weight (%)
C	5.9
O	42.5
Na	1.6
Mg	1.2
Al	9.1
Si	30
K	2.2
Ca	**0.8**
Fe	5.1

(a)

Element	Weight (%)
C	4.1
O	37.4
Na	0.5
Mg	0.7
Al	5.5
Si	33.1
K	1.0
Ca	**1.8**
Fe	5.1

(b)

Element	Weight (%)
C	1.5
O	29.1
Mg	0.6
Al	9.2
Si	40.7
Cl	2.8
K	2.4
Ca	**4.7**
Fe	9.9

(c)

(d)
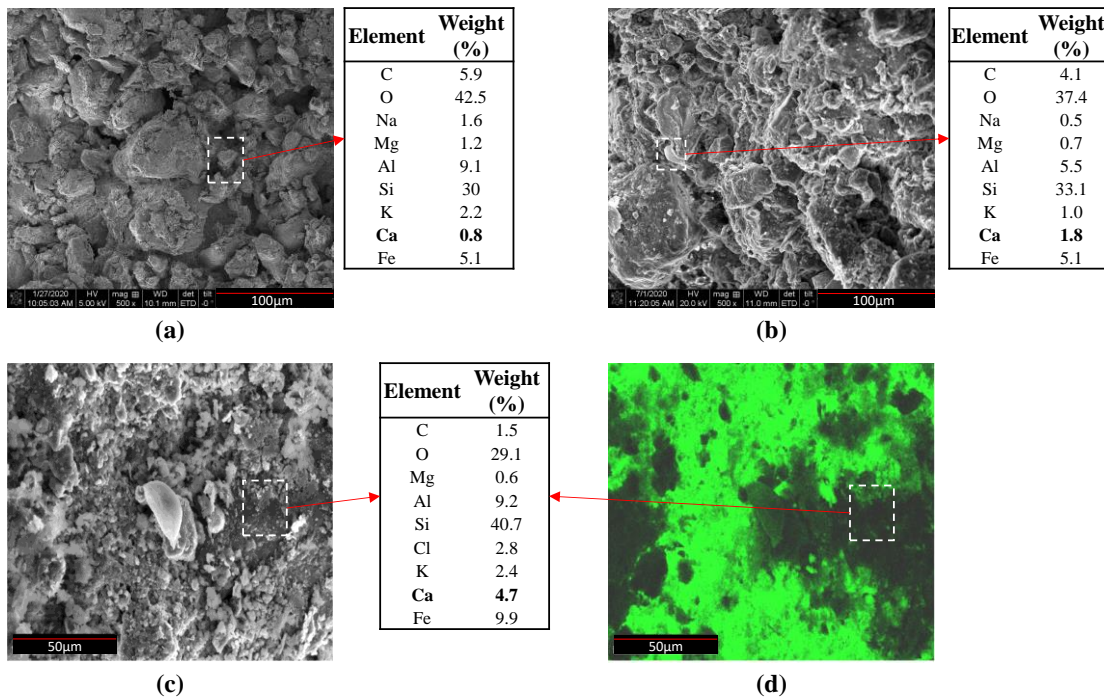
Figure 12. SEM imaging and EDS results of (a) untreated, (b) UB-treated, and (c) UBC-treated samples; and (d) calcium element mapping of the UBC-treated sample.

5.1.6. XRD and Raman Spectra

The XRD spectra in Figure 13 present the mineral compositions of the silt samples without treatment and with UBC treatment. The XRD pattern of the untreated silt sample shown in Figure 13a indicates a high mass percentage of quartz and relatively small amounts of albite, muscovite, and glauconite. The XRD pattern of the UBC-treated sample demonstrates a similar pattern as the untreated silt sample, including quartz, albite, muscovite, and glauconite. It can be seen that XRD can not detect the mineral changes after the UBC treatment since the XRD has a detection limit of about 2% to 3% mass percentage of a mineral (*57; 58*). Since the amount of equivalent $CaCO_3$

precipitation is below 1% in this study, the XRD analysis could not detect the mineral changes in the silt samples after MICP treatment.

(a)

(b)
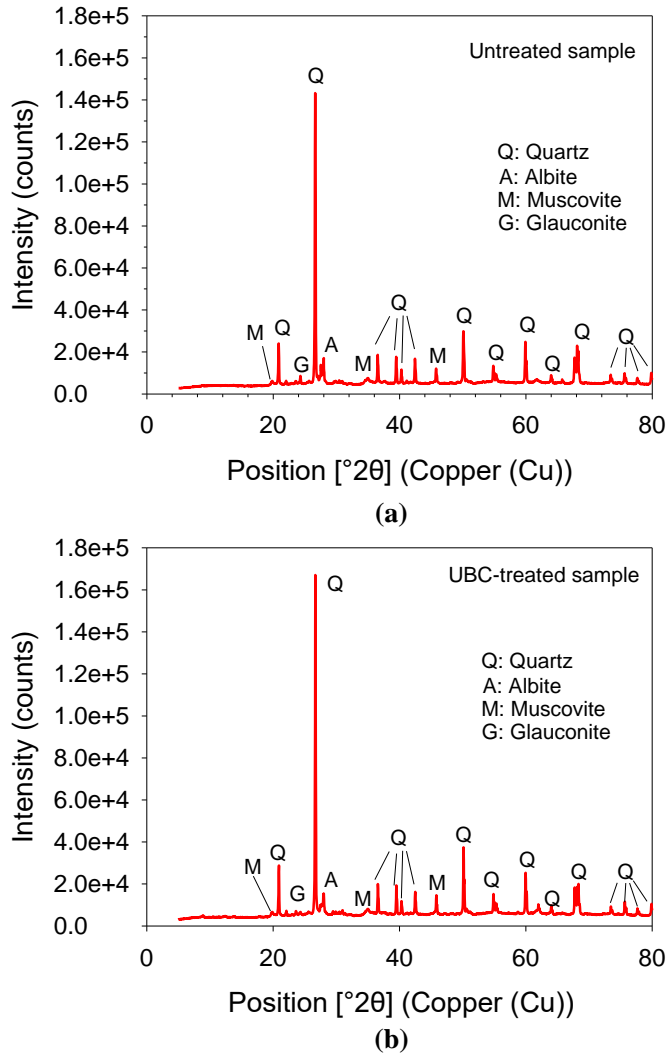
Figure 13. X-Ray Diffraction (XRD) patterns of (a) untreated and (b) UBC-treated samples.
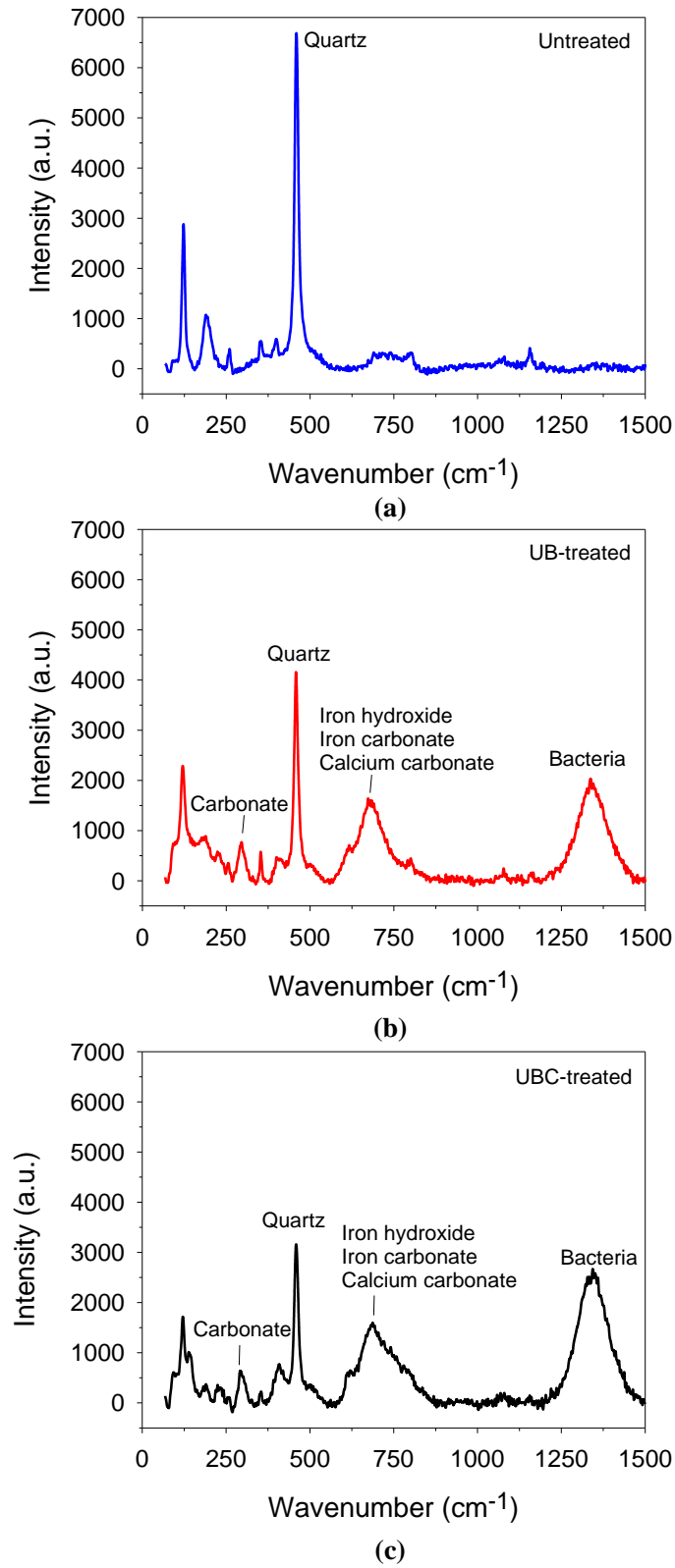
Figure 14. Raman spectra of (a) untreated, (b) UB-treated, and (c) UBC-treated samples.

Figure 14 shows the Raman spectra of the untreated, UB-treated, and UBC-treated samples. The Raman spectrum of the untreated sample (Figure 14a) shows a high-intensity peak at 460 cm^{-1}, indicating quartz in the silt (*59*), which is also confirmed by the XRD spectra shown in Figures 13a and b. The peaks in the range of 90 to 430 cm^{-1} of the Raman spectrum of the untreated sample correspond to many other minerals (containing magnesium and iron) in the soil. However, it is impossible to define their corresponding minerals due to the complexity of the measured peaks and soil minerals. As compared to the Raman spectrum of the untreated sample, the Raman spectra of the UB-treated and UBC-treated samples show several additional peaks. The peaks located at 296 cm^{-1} indicate carbonate, which matches the typical Raman spectra of carbonate (*60; 61*). A broad peak covering from 580 to 850 cm^{-1} corresponds to the minerals of iron hydroxide, iron carbonate, and calcium carbonate in the literature studies (*62-66*). These results confirm the precipitation of calcium carbonate, iron hydroxide, and iron carbonate in the silt samples during MICP treatment. In addition, the peak observed at the 1340 cm^{-1} is related to the bacteria cells added in the silt in accordance with previous literature studies (*67*). The results of the Raman spectra demonstrate that there were iron hydroxide, iron carbonate, and calcium carbonate precipitations in the silt samples during the UB and UBC treatments. The calcium carbonate precipitation may be limited in the UB-treated samples as no cementation medium (i.e., calcium chloride) was added.

5.1.7. Discussions

Most research on MICP used calcium cation (e.g., calcium chloride) to induce $CaCO_3$ precipitation for cementing soil matrix (*11; 20; 68*). However, other types of cementation compounds could also be produced from the MICP treatment, such as ferrous carbonate ($FeCO_3$), ferric hydroxide ($Fe(OH)_3$), and ferric carbonate ($Fe_2(CO_3)_3$) (*15*). Naeimi, Chu and Haddad (*51)* used the ferrous cations (provided by ferrous sulfate) to replace calcium cation in the MICP treatment to precipitate ferrous carbonate ($FeCO_3$) in a poorly graded medium-grained clean sand. The results showed that the unconfined compressive strength increased up to 402 kPa at the ferrous carbonate content of 6%. The precipitated ferrous carbonates were found cementing sand grains in the SEM imaging. Ivanov, Chu and Stabnikov (*69)* used the iron-based biogrout that consists of urease-producing bacteria, ferric cations (provided by ferric chelate), and urea to precipitate ferric hydroxide ($Fe(OH)_3$) for improving the strength and reducing the permeability of a rounded-grain silica sand. The unconfined compressive strength increased with the increasing ferric hydroxide content and reached 240 kPa at the ferric hydroxide content of 3%.

Since iron exists in the test silt as evidenced by the EDS analysis (ranged from 5.1 to 9.9% shown in Figure 12), it is possible that several iron precipitations (e.g., iron carbonate and iron hydroxide) were formed in the silt samples during the UB and UBC treatments. This possibility was also confirmed by the Raman spectra (Figure 14), which shows a new peak (from 580 to 850 cm^{-1}) that indicates the presence of iron hydroxide, iron carbonate, and calcium carbonate generated in the UB-and UBC-treated samples. Because of the generation of the iron precipitation compounds, the UB-treated samples had higher shear strength than those of the untreated silt samples in the direct shear tests. When adding cementation medium in the UBC-treated samples, the precipitations of $CaCO_3$ and iron compounds lead to higher shear strengths than those of UB-treated samples. Thus, the $CaCO_3$ content measurements in Figure 10 are measurements of the equivalent $CaCO_3$ contents as the iron carbonate was precipitated in the silt samples. In addition, the increasing shear strengths of the UB-and UBC-treated samples may also be attributed to the increasing pH, which may result in osmotic effects in the clay portion of the silt samples (*70; 71*).

5.2. Wetting and Drying Cycle Tests

Figure 15 shows the binary photos of cracks of each sample. Figures 15a to c show the cracks generated in each sample during Treatment 0. Figures 15d to f show the cracks of each sample during Treatment 1. Figures 15g to i show the cracks of each sample during Treatment 2 (performed MICP treatment). Figures 15j to l show the cracks of each sample during Treatment 3. Figures 15a to f shows that Treatment 1 wetting-drying cycle induced new branches of cracks along the existing cracks as compared to Treatment 0. Comparing the treated (Figures 15g to i) with untreated samples (Figures 15d to f), it can be observed that the crack width of certain cracks and crack areas decreased. From Treatment 2 to Treatment 3, the number of cracks and crack areas of Figures 15j to l (Treatment 3) increased compared to Figures 15g to i (Treatment 2). This demonstrates that the number of cracks and areas after MICP treatment can still increase to some extent if wetting-drying cycles continued, which needs further investigation in future studies.
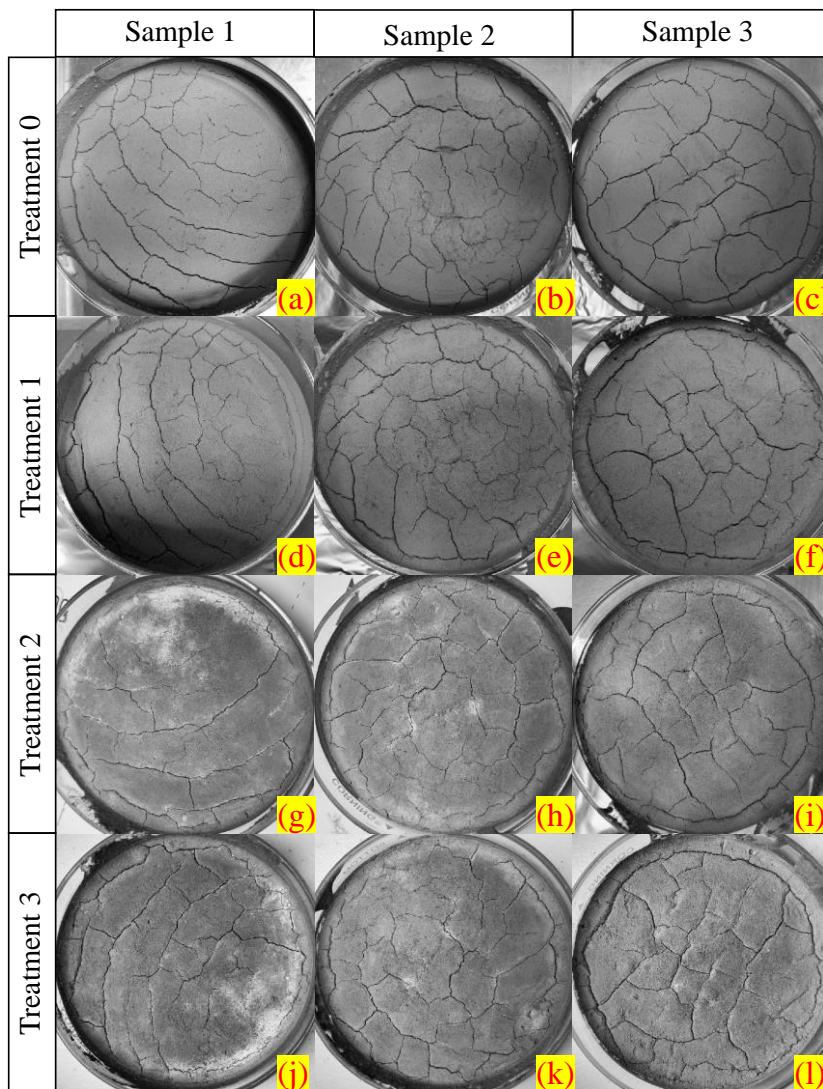
Figure 15. Photos of the soil cracks: (a) sample 1 at treatment 0, (b) sample 2 at treatment 0, (c) sample 3 at treatment 0, (d) sample 1 at treatment 1, (e) sample 2 at treatment 1, (f) sample 3 at treatment 1, (g) sample 1 at treatment 2, (h) sample 2 at treatment 2, (i) sample 3 at treatment 2, (j) sample 1 at treatment 3, (k) sample 2 at treatment 3, (l) sample 3 at treatment 3.
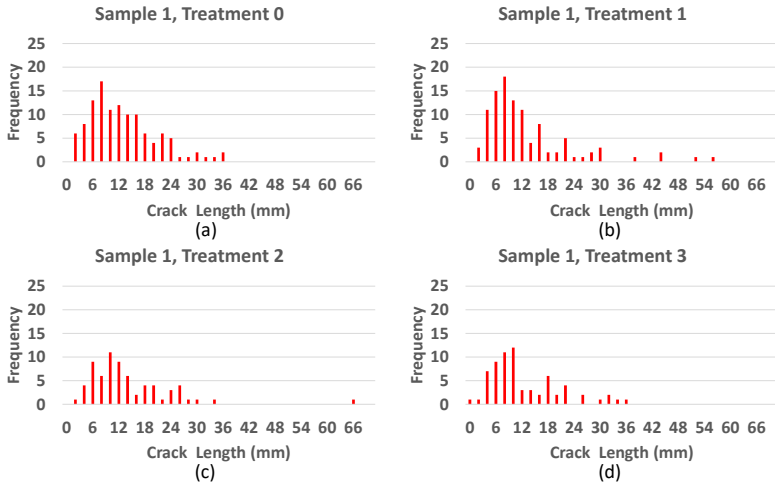
Figure 16. Statistical results of the crack length of sample 1 at each treatment cycle.
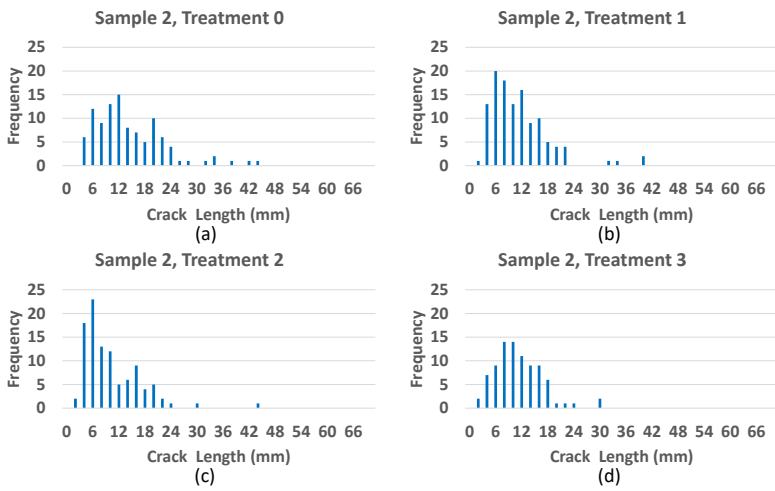
Figure 17. Statistical results of the crack length of sample 2 at each treatment cycle.
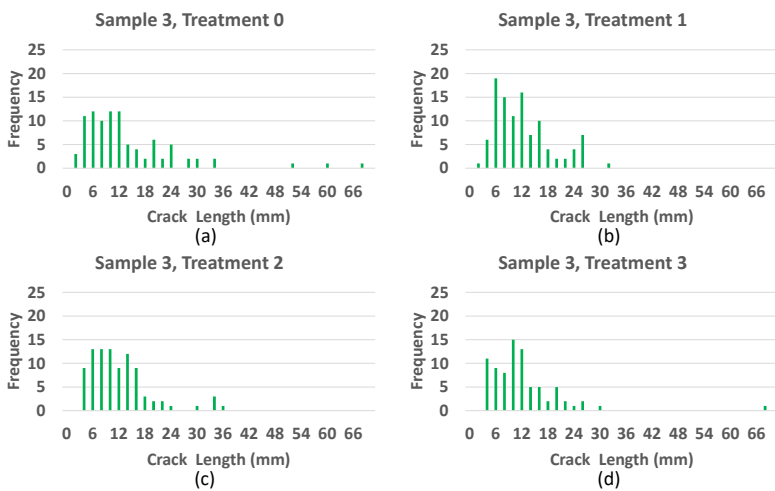
Figure 18. Statistical results of the crack length of sample 3 at each treatment cycle.

The distributions of the measured crack lengths at different treatment cycles were summarized in Figures 16 to 18. The y-axis (frequency) corresponds to the number of cracks generated in the designated crack length range (defined on the x-axis). The crack length and frequency in each sample were slightly increased from Treatment 0 to Treatment 1, respectively (Figures a to b in Figures 16, 17, and 18). Comparing the distribution of crack lengths between Treatment 1 (before MICP treatment, Figures 16b, 17b, and 18b) and Treatment 2 (after MICP treatment, Figures 16c, 17c, and 18c), the frequencies of the cracks in most crack length ranges were significantly reduced. These reductions are mainly attributed to the $CaCO_3$ precipitation during MICP treatment that healed the desiccation cracks.
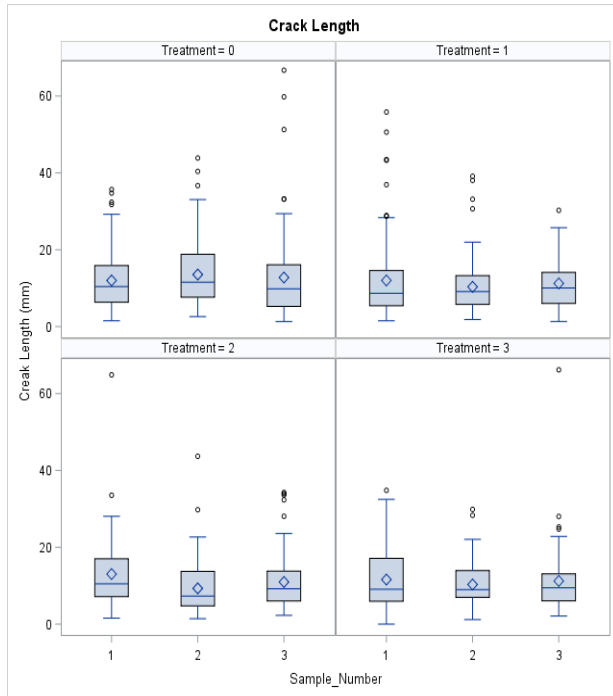
(a)
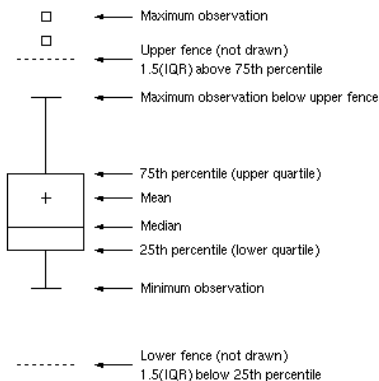
(b)

Figure 19. (a) Box plots of crack length versus treatment, (b) box plot legend.

28
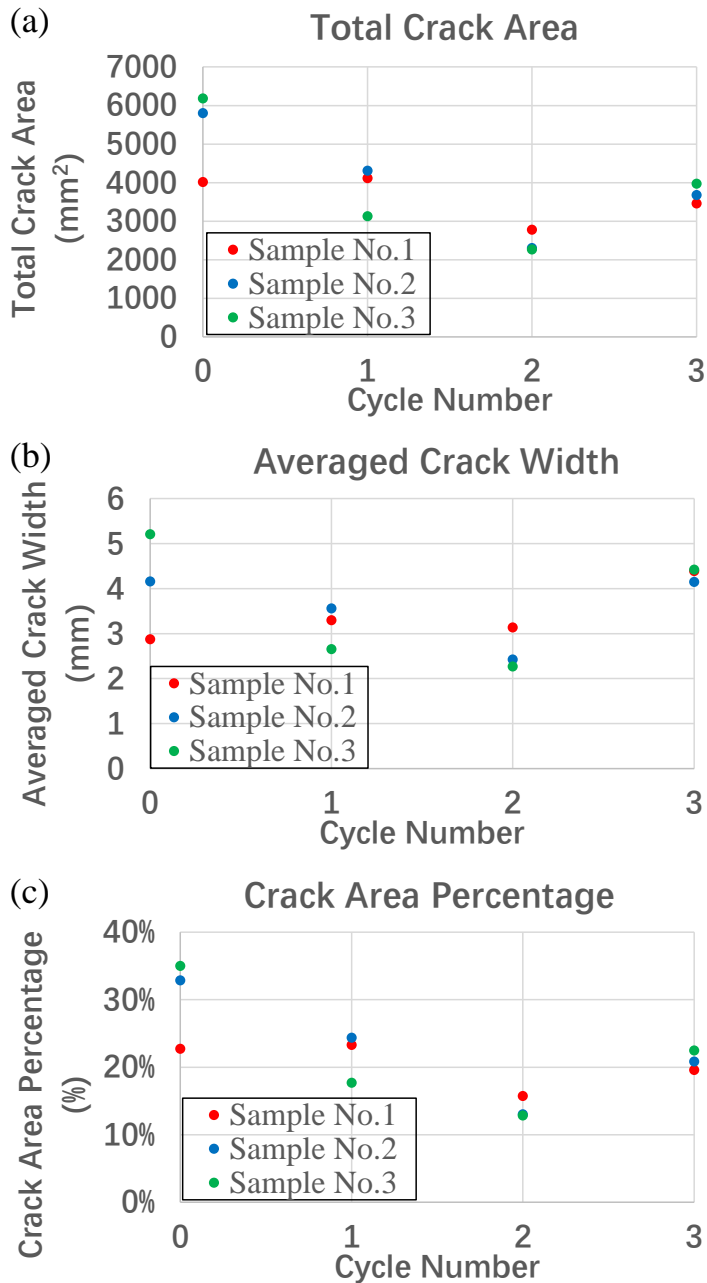
Figure 20. (a) Average crack area versus treatment, (b) average crack width versus treatment, and (c) average crack percentage versus treatment.

Figure 19 summarizes the statistical data of crack lengths of three samples during different treatment cycles. In Figure 19a, it seems that the mean values of the crack length did not show a significant decrease after MICP treatment (comparison between Treatment cycle 1 and Treatment cycle 2). However, as shown in Treatment cycles 2 and 3, the number of outliers were significantly reduced compared to Treatment cycles 0 and 1, demonstrating that MICP treatment can reduce the crack length, especially those long cracks. Figure 19b shows the box plot legend of Figure 19a. As shown in Figures 20a, b, and c, there are decreasing trends of total crack area, averaged crack

width, and crack area percentage from Treatment 0 to Treatment 2. It is unclear why the total crack area, averaged crack width, and crack area percentage decreased from Treatment 0 to Treatment 1. This may be due to the erosion induced by deionized water application during wetting stage, which eroded the surface soil to fill the cracks. For the trends from Treatments 1 to 2 (from untreated cycle to MICP-treated cycle) in Figures 20a, b, and c, the decreases of the total crack area, averaged crack width, and crack area percentage are due to carbonate precipitation (evidenced by the white $CaCO_3$ shown in the cracks). After the MICP treatment, there was an increasing trend from Treatment 2 to Treatment 3. This trend also confirms the previous observations of the crack length (increasing for Treatment 2 to Treatment 3) in Figures 16 through 18. It can be concluded that the MICP treatment can heal the desiccation cracks of low-plasticity silt in a relatively short period. It is also important to note that the cracks could regenerate after MICP treatment, as evidenced by the increasing crack parameters from Treatment 2 to Treatment 3 (Figures 4.8a to c). Future studies will focus on optimizing MICP treatment solutions and schedule to reduce the formation of cracks after MICP treatment.
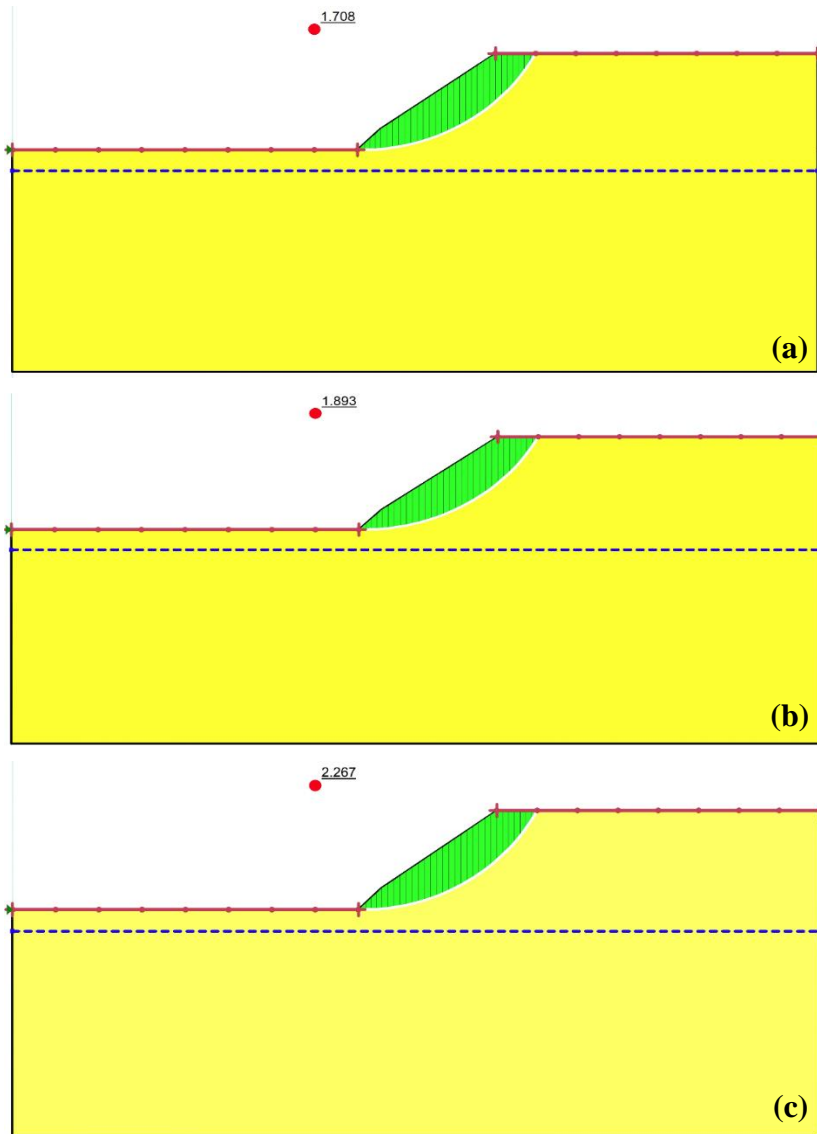
Figure 21. SLOPE/W analysis results: (a) untreated slope, (b) UB-treated slope, and (c) UBC-treated slope.

5.3. Preliminary Slope Stability Modeling

The results of the SLOPE/W analysis are shown in Figure 21. When comparing the failure surfaces among Figures 21a, b, and c, the affected soil areas (green areas in Figure 21) are almost identical. The factor of safety of the original untreated embankment slope is 1.708 as shown in Figure 21a. Figures 21b and c show the results of the UB-treated and UBC-treated slopes, respectively. The factor of safety of the UB-treated slope is 1.893, which is 12% higher than the untreated slope as shown in Table 4. When compared to the UB-treated slope, the factor of safety of the UBC-treated slope is 2.267 (21% higher). Also, the factor of safety of the UBC-treated slope is 33% higher than untreated slope.

Table 4. SLOPE/W results.

Treatment Types	Factor of Safety	Increment
Untreated	1.7	
UB-treated	1.9	+12%
UBC-treated	2.3	+21%

5.4. Field Test

The research team is planning a field test of using bio-cement to seal slope cracks and increase slope stability. The site is located along Highway 66 in St. Francisville, Louisiana (Figure 22a). The highway embankment slope at the site has been showing slope stability issues since 2017. The current site conditions are shown in Figures 22b and c. Surface cracks were observed on the highway (Figure 22c). Two inclinometers were installed at the site for monitoring the slope movement. The research team plans to percolate bio-grout solutions into the cracks on the highway embankment. Initially, 10 gallons of bio-grout solutions will be percolated into the cracks. Inclinometer measurements will be regularly performed to monitor the slope movement after bio-grout treatment.

Figure 22. (a) Field test site location, (b) highway embankment slope, and (c) cracks on the highway.

6. CONCLUSIONS

Through a combination of experimental studies and SLOPE/W analysis, the research described in this thesis evaluated the potential effectiveness of MICP treatment for improving the mechanical properties of low-plasticity silt, healing desiccation cracks, and enhancing the stability of embankment slopes. Geotechnical laboratory tests included direct shear tests and cyclic wetting-drying tests. A preliminary slope stability analysis was conducted using SLOPE/W. Scanning electron microscopy (SEM) imaging, energy-dispersive X-ray spectroscopy (EDS), X-ray Powder Diffraction (XRD), and Raman spectroscopy analysis were used to investigate the soil morphology and the elemental compositions of the soil. Based on the results presented in this thesis, the following conclusions are drawn.

- The peak and ultimate shear strengths of the silt samples were improved by the UB and UBC treatments. The peak shear strengths increased by an average of 12% for the UB-treated samples and 30% for the UBC-treated samples compared to the peak shear strengths of the untreated samples.
- UB-and UBC-treated samples showed lower vertical compression displacements than the untreated samples. UB-treated samples generally showed fewer settlements as compared to the UBC-treated samples. The different compression displacements between different treatments are controlled by the distribution of equivalent $CaCO_3$ contents in the samples.
- The peak friction angles of the untreated, UB-treated, and UBC-treated samples are 28.8°, 33.9°, and 37.6°, respectively. The cohesions of the untreated, UB-treated, and UBC-treated samples are 5.9, 5.4, and 7.1 kPa, respectively.
- The improvements of the mechanical properties of the UB-and UBC-treated samples can likely be attributed to the precipitations of calcium carbonate, iron carbonate, and iron hydroxide at the shear interface. Higher equivalent $CaCO_3$ contents at the shear interface were measured in the UBC-treated samples, leading to higher peak shear strengths of the UBC-treated samples.
- Since iron exists in the silt as evidenced by the EDS analysis, it is possible that several iron precipitations (e.g., iron carbonate and iron hydroxide) were formed in the silt samples during the UB and UBC treatments. The precipitations of iron carbonate and iron hydroxide were also confirmed by the Raman spectra of the UB-and UBC-treated samples.
- The MICP treatment has the potential to heal desiccation cracks as evidenced by the cyclic wetting-drying tests. In the preliminary tests reported here, MICP treatment can reduce the crack length, especially those long cracks. Also, total crack area, averaged crack width, and crack area percentage decreased by 32%, 15%, and 36%, respectively.
- The results of the SLOPE/W analysis show that MICP treatment could potentially enhance slope stability by increasing the factor of safety from 1.7 to 2.3 for the test case considered. The MICP treatment had a positive effect on the improvement of slope stability; however, further investigation is needed. A future large-scale experimental or field-scale study is recommended to optimize the treatment solutions and procedures, assess the improvement quality, and investigate long-term effect of MICP treatment.
- Collectively, the research reported in this thesis suggests that MICP treatment can improve the engineering properties of low-plasticity silt, heal desiccation cracks, and enhance slope factor. It is recommended that future studies should focus on the optimization of MICP treatment for in-situ slope stabilization and ground improvement.

REFERENCES

1. Yang, L., C. Kaisheng, L. Mengfei, and W. Yingchao. Study on failure of red clay slopes with different gradients under dry and wet cycles. *Bulletin of Engineering Geology and the Environment,* Vol. 79, 2020, pp. 4609-4624.

2. Clarke, D., and J. Smethurst. Effects of climate change on cycles of wetting and drying in engineered clay slopes in England. *Quarterly Journal of Engineering Geology and Hydrogeology,* Vol. 43, No. 4, 2010, pp. 473-486.

3. Wang, Z., Q. Li, N. Zhang, Y. Jin, H. Qin, and J. Ding. Slope failure of biotreated sand embankments under rainfall conditions: experimental investigation and numerical simulation. *Bulletin of Engineering Geology and the Environment,* Vol. 79, No. 9, 2020, pp. 4683-4699.

4. Whiffin, V. S., L. A. Van Paassen, and M. P. Harkes. Microbial carbonate precipitation as a soil improvement technique. *Geomicrobiology Journal,* Vol. 24, No. 5, 2007, pp. 417-423.

5. DeJong, J. T., M. B. Fritzges, and K. Nüsslein. Microbially induced cementation to control sand response to undrained shear. *Journal of geotechnical and geoenvironmental engineering,* Vol. 132, No. 11, 2006, pp. 1381-1392.

6. Chu, J., V. Ivanov, J. He, M. Naeimi, B. Li, and V. Stabnikov. Development of microbial geotechnology in Singapore.In *Geo-Frontiers 2011: Advances in Geotechnical Engineering*, 2011. pp. 4070-4078.

7. Chou, C.-W., E. A. Seagren, A. H. Aydilek, and M. Lai. Biocalcification of sand through ureolysis. *Journal of geotechnical and geoenvironmental engineering,* Vol. 137, No. 12, 2011, pp. 1179-1189.

8. DeJong, J. T., B. M. Mortensen, B. C. Martinez, and D. C. Nelson. Bio-mediated soil improvement. *Ecological Engineering,* Vol. 36, No. 2, 2010, pp. 197-210.

9. Al Qabany, A., and K. Soga. Effect of chemical treatment used in MICP on engineering properties of cemented soils.In *Bio-and Chemo-Mechanical Processes in Geotechnical Engineering: Géotechnique Symposium in Print 2013*, ICE Publishing, 2014. pp. 107-115.

10. van Paassen, L. A., R. Ghose, T. J. van der Linden, W. R. van der Star, and M. C. van Loosdrecht. Quantifying biomediated ground improvement by ureolysis: large-scale biogrout experiment. *Journal of geotechnical and geoenvironmental engineering,* Vol. 136, No. 12, 2010, pp. 1721-1728.

11. Mortensen, B., M. Haber, J. DeJong, L. Caslake, and D. Nelson. Effects of environmental factors on microbial induced calcium carbonate precipitation. *Journal of applied microbiology,* Vol. 111, No. 2, 2011, pp. 338-349.

12. Burbank, M., T. Weaver, R. Lewis, T. Williams, B. Williams, and R. Crawford. Geotechnical tests of sands following bioinduced calcite precipitation

catalyzed by indigenous bacteria. *Journal of geotechnical and geoenvironmental engineering,* Vol. 139, No. 6, 2013, pp. 928-936.

13. Martinez, B., J. DeJong, T. Ginn, B. Montoya, T. Barkouki, C. Hunt, B. Tanyu, and D. Major. Experimental optimization of microbial-induced carbonate precipitation for soil improvement. *Journal of geotechnical and geoenvironmental engineering,* Vol. 139, No. 4, 2013, pp. 587-598.

14. Stark, T. D., P. J. Ricciardi, and R. D. Sisk. Case study: Vertical drain and stability analyses for a compacted embankment on soft soils. *Journal of geotechnical and geoenvironmental engineering,* Vol. 144, No. 2, 2018, p. 05017007.

15. Ivanov, V., and J. Chu. Applications of microorganisms to geotechnical engineering for bioclogging and biocementation of soil in situ. *Reviews in Environmental Science and Bio/Technology,* Vol. 7, No. 2, 2008, pp. 139-153.

16. Fujita, Y., J. L. Taylor, T. L. Gresham, M. E. Delwiche, F. S. Colwell, T. L. McLing, L. M. Petzke, and R. W. Smith. Stimulation of microbial urea hydrolysis in groundwater to enhance calcite precipitation. *Environmental science & technology,* Vol. 42, No. 8, 2008, pp. 3025-3032.

17. Harkes, M. P., L. A. Van Paassen, J. L. Booster, V. S. Whiffin, and M. C. van Loosdrecht. Fixation and distribution of bacterial activity in sand to induce carbonate precipitation for ground reinforcement. *Ecological Engineering,* Vol. 36, No. 2, 2010, pp. 112-117.

18. Van Paassen, L. A. Biogrout, ground improvement by microbial induced carbonate precipitation. 2009.

19. Cheng, L., R. Cord-Ruwisch, and M. A. Shahin. Cementation of sand soil by microbially induced calcite precipitation at various degrees of saturation. *Canadian Geotechnical Journal,* Vol. 50, No. 1, 2013, pp. 81-90.

20. Rebata-Landa, V. Microbial activity in sediments: effects on soil behavior.In*, No. PhD Thesis*, Georgia Institute of Technology, 2007.

21. Yun, T. S., and J. C. Santamarina. Decementation, softening, and collapse: changes in small-strain shear stiffness in k 0 loading. *Journal of geotechnical and geoenvironmental engineering,* Vol. 131, No. 3, 2005, pp. 350-358.

22. Cheng, L., and R. Cord-Ruwisch. Upscaling effects of soil improvement by microbially induced calcite precipitation by surface percolation. *Geomicrobiology Journal,* Vol. 31, No. 5, 2014, pp. 396-406.

23. Montoya, B., J. DeJong, and R. Boulanger. Dynamic response of liquefiable sand improved by microbial-induced calcite precipitation.In *Bio-and Chemo-Mechanical Processes in Geotechnical Engineering: Géotechnique Symposium in Print 2013*, ICE Publishing, 2014. pp. 125-135.

24. Lin, H., M. T. Suleiman, D. G. Brown, and E. Kavazanjian Jr. Mechanical behavior of sands treated by microbially induced carbonate precipitation. *Journal*

of geotechnical and geoenvironmental engineering, Vol. 142, No. 2, 2016, p. 04015066.

25. Lin, H., M. T. Suleiman, H. M. Jabbour, and D. G. Brown. Bio-grouting to enhance axial pull-out response of pervious concrete ground improvement piles. *Canadian Geotechnical Journal,* Vol. 55, No. 1, 2018, pp. 119-130.

26. Terzis, D., and L. Laloui. Cell-free soil bio-cementation with strength, dilatancy and fabric characterization. *Acta Geotechnica,* Vol. 14, No. 3, 2019, pp. 639-656.

27. Lin, H., S. T. O'Donnell, M. T. Suleiman, E. Kavazanjian Jr, and D. G. Brown. Effects of Enzyme and Microbially Induced Carbonate Precipitation Treatments on the Response of Axially Loaded Pervious Concrete Piles. *Journal of geotechnical and geoenvironmental engineering,* Vol. 147, No. 8, 2021, p. 04021057.

28. Soon, N. W., L. M. Lee, T. C. Khun, and H. S. Ling. Factors affecting improvement in engineering properties of residual soil through microbial-induced calcite precipitation. *Journal of geotechnical and geoenvironmental engineering,* Vol. 140, No. 5, 2014, p. 04014006.

29. Li, B. Geotechnical properties of biocement treated sand and clay.In *School of Civil and Environmental Engineering, No. Ph.D. thesis*, Nanyang Technological University, Singapore, 2015.

30. Islam, M. T., B. C. Chittoori, and M. Burbank. Evaluating the applicability of biostimulated calcium carbonate precipitation to stabilize clayey soils. *Journal of Materials in Civil Engineering,* Vol. 32, No. 3, 2020, p. 04019369.

31. Mitchell, J. K., and J. C. Santamarina. Biological considerations in geotechnical engineering. *Journal of geotechnical and geoenvironmental engineering,* Vol. 131, No. 10, 2005, pp. 1222-1233.

32. Arpajirakul, S., W. Pungrasmi, and S. Likitlersuang. Efficiency of microbially-induced calcite precipitation in natural clays for ground improvement. *Construction and Building Materials,* Vol. 282, 2021, p. 122722.

33. He, J., Y. Gao, Z. Gu, J. Chu, and L. Wang. Characterization of crude bacterial urease for CaCO 3 precipitation and cementation of silty sand. *Journal of Materials in Civil Engineering,* Vol. 32, No. 5, 2020, p. 04020071.

34. Sharma, A., and R. Ramkrishnan. Study on effect of microbial induced calcite precipitates on strength of fine grained soils. *Perspectives in Science,* Vol. 8, 2016, pp. 198-202.

35. Won, J., B. Jeong, J. Lee, S. Dai, and S. E. Burns. Facilitation of microbially induced calcite precipitation with kaolinite nucleation. *Geotechnique,* Vol. 71, No. 8, 2021, pp. 728-734.

36. Cardoso, R., I. Pires, S. O. Duarte, and G. A. Monteiro. Effects of clay's chemical interactions on biocementation. *Applied Clay Science,* Vol. 156, 2018, pp. 96-103.

37. Wang, Z., J. Li, and L. Zhang. Influence of cracks on the stability of a cracked soil slope.In *Proc., 5th Asia-Pacisif Conf. on Unsaturated Soils (AP-UNSAT 2011)*, 2011. pp. 721-728.

38. Gray, D. H., and A. T. Leiser. *Biotechnical slope protection and erosion control*. Van Nostrand Reinhold Company Inc., 1982.

39. Wu, T. H., M. M. Riestenberg, and A. Flege. *Root properties for design of slope stabilization*. Thomas Telford, London, 1995.

40. Duncan, J. M., S. G. Wright, and T. L. Brandon. *Soil strength and slope stability*. John Wiley & Sons, 2014.

41. Smith, R., and R. Peck. Stabilization by pressure grouting on American railroads. *Geotechnique,* Vol. 5, No. 3, 1955, pp. 243-252.

42. Purbrick, M., and D. Ayres. USES OF AERATED CEMENT GROUT AND MORTAR IN STABILIZATION OF SLIPS IN EMBANKMENTS, LARGE-SCALE TUNNEL REPAIRS, AND OTHER WORKS. *Proceedings of the Institution of Civil Engineers,* Vol. 5, No. 1, 1956, pp. 52-75.

43. Arya, I., I. Wiraga, and I. G. Suryanegara. Effect of cement injection on sandy soil slope stability, case study: slope in Petang district, Badung regency.In *Journal of Physics: Conference Series, No. 953*, IOP Publishing, 2018. p. 012103.

44. Vail, M., C. Zhu, C.-S. Tang, L. Anderson, M. Moroski, and M. T. Montalbo-Lomboy. Desiccation cracking behavior of MICP-treated bentonite. *Geosciences,* Vol. 9, No. 9, 2019, p. 385.

45. Mitchell, J. K., and K. Soga. *Fundamentals of soil behavior*. John Wiley & Sons New York, 2005.

46. Jang, J., and J. C. Santamarina. Fines classification based on sensitivity to pore-fluid chemistry. *Journal of geotechnical and geoenvironmental engineering,* Vol. 142, No. 4, 2016, p. 06015018.

47. Park, J., and J. C. Santamarina. Revised soil classification system for coarse-fine mixtures. *Journal of geotechnical and geoenvironmental engineering,* Vol. 143, No. 8, 2017, p. 04017039.

48. Cho, G. C., J. Dodds, and J. C. Santamarina. Particle shape effects on packing density, stiffness, and strength: natural and crushed sands. *J. Geotech. Geoenviron. Eng.*, 2006, pp. 591-602.

49. ASTM. Standard test method for direct shear of soils under consolidated drained conditions.In *ASTM D3080*, West Conshohocken, PA, 2003.

50. ---. Standard test method for rapid determination of carbonate content soils.In *ASTM D4373,*, West Conshohocken, PA, 2014.

51. Naeimi, M., J. Chu, and A. Haddad. Comparison of Chemical Source and Microbially Produced Ferrous Cations for Iron-Based Biocementation of Sand. *Iranian Journal of Science and Technology, Transactions of Civil Engineering,* Vol. 40, No. 2, 2016, pp. 149-157.

52. Liu, C., C.-S. Tang, B. Shi, and W.-B. Suo. Automatic quantification of crack patterns by image processing. *Computers & Geosciences,* Vol. 57, 2013, pp. 77-80.

53. Morgenstern, N. u., and V. E. Price. The analysis of the stability of general slip surfaces. *Geotechnique,* Vol. 15, No. 1, 1965, pp. 79-93.

54. Martinez, B. C., and J. T. DeJong. Bio-mediated soil improvement: load transfer mechanisms at the micro-and macro-scales.In *Advances in ground improvement: research to practice in the United States and China*, 2009. pp. 242-251.

55. Terzis, D., and L. Laloui. 3-D micro-architecture and mechanical response of soil cemented via microbial-induced calcite precipitation. *Scientific reports,* Vol. 8, No. 1, 2018, pp. 1-11.

56. Lin, H., M. T. Suleiman, and D. G. Brown. Investigation of Pore-Scale CaCO3 Distributions and Their Effects on Stiffness and Permeability of Sands Treated by Microbially Induced Carbonate Precipitation (MICP). *Soils and Foundations,* Vol. 60, No. 4, 2020, pp. 944-961.

57. Moore, D. M., and R. C. Reynolds Jr. *X-ray Diffraction and the Identification and Analysis of Clay Minerals*. Oxford University Press (OUP), 1989.

58. Newman, J. A., P. D. Schmitt, S. J. Toth, F. Deng, S. Zhang, and G. J. Simpson. Parts per million powder X-ray diffraction. *Analytical chemistry,* Vol. 87, No. 21, 2015, pp. 10950-10955.

59. Goienaga, N., N. Arrieta, J. Carrero, M. Olivares, A. Sarmiento, I. Martinez-Arkarazo, L. Fernández, and J. Madariaga. Micro-Raman spectroscopic identification of natural mineral phases and their weathering products inside an abandoned zinc/lead mine. *Spectrochimica acta Part A: Molecular and biomolecular spectroscopy,* Vol. 80, No. 1, 2011, pp. 66-74.

60. Steele, A., M. Fries, H. Amundsen, B. Mysen, M. Fogel, M. Schweizer, and N. Boctor. Comprehensive imaging and Raman spectroscopy of carbonate globules from Martian meteorite ALH 84001 and a terrestrial analogue from Svalbard. *Meteoritics & Planetary Science,* Vol. 42, No. 9, 2007, pp. 1549-1566.

61. Zhao, C., L. Xu, W. Gui, and J. Liu. Phase Stability and Vibrational Properties of Iron-Bearing Carbonates at High Pressure. *Minerals,* Vol. 10, No. 12, 2020, p. 1142.

62. De Faria, D., S. Venâncio Silva, and M. De Oliveira. Raman microspectroscopy of some iron oxides and oxyhydroxides. *Journal of Raman spectroscopy,* Vol. 28, No. 11, 1997, pp. 873-878.

63. Hanesch, M. Raman spectroscopy of iron oxides and (oxy) hydroxides at low laser power and possible applications in environmental magnetic studies. *Geophysical Journal International,* Vol. 177, No. 3, 2009, pp. 941-948.

64. De La Pierre, M., C. Carteret, L. Maschio, E. André, R. Orlando, and R. Dovesi. The Raman spectrum of CaCO3 polymorphs calcite and aragonite: a

combined experimental and computational study. *The Journal of Chemical Physics,* Vol. 140, No. 16, 2014, p. 164509.

65. Spivak, A., N. Solopova, V. Cerantola, E. Bykova, E. Zakharchenko, L. Dubrovinsky, and Y. Litvin. Raman study of MgCO 3–FeCO 3 carbonate solid solution at high pressures up to 55 GPa. *Physics and Chemistry of Minerals,* Vol. 41, No. 8, 2014, pp. 633-638.

66. Dufresne, W. J., C. J. Rufledt, and C. P. Marshall. Raman spectroscopy of the eight natural carbonate minerals of calcite structure. *Journal of Raman spectroscopy,* Vol. 49, No. 12, 2018, pp. 1999-2007.

67. Parikh, S. J., K. W. Goyne, A. J. Margenot, F. N. Mukome, and F. J. Calderón. Soil chemical insights provided through vibrational spectroscopy. *Advances in agronomy,* Vol. 126, 2014, pp. 1-148.

68. DeJong, J., K. Soga, E. Kavazanjian, S. Burns, L. Van Paassen, A. Al Qabany, A. Aydilek, S. Bang, M. Burbank, and L. F. Caslake. Biogeochemical processes and geotechnical applications: progress, opportunities and challenges.In *Bio-and Chemo-Mechanical Processes in Geotechnical Engineering: Géotechnique Symposium in Print 2013*, Ice Publishing, 2014. pp. 143-157.

69. Ivanov, V., J. Chu, and V. Stabnikov. Iron-and calcium-based biogrouts for porous soils. *Proceedings of the Institution of Civil Engineers-Construction Materials,* Vol. 167, No. 1, 2014, pp. 36-41.

70. Calvello, M., M. Lasco, R. Vassallo, and C. Di Maio. Compressibility and residual shear strength of smectitic clays: influence of pore aqueous solutions and organic solvents. *Italian Geotechnical Journal,* Vol. 1, No. 2005, 2005, pp. 34-46.

71. Spagnoli, G., D. Rubinos, H. Stanjek, T. Fernández-Steeger, M. Feinendegen, and R. Azzam. Undrained shear strength of clays as modified by pH variations. *Bulletin of Engineering Geology and the Environment,* Vol. 71, No. 1, 2012, pp. 135-148.